Monthly Notices
of the
ROYAL ASTRONOMICAL SOCIETY

MNRAS **464,** 3597–3616 (2017) doi:10.1093/mnras/stw2407
Advance Access publication 2016 September 22

IMF and [Na/Fe] abundance ratios from optical and NIR spectral features in early-type galaxies

F. La Barbera,[1⋆] A. Vazdekis,[2,3⋆] I. Ferreras,[4⋆] A. Pasquali,[5] C. Allende Prieto,[2,3] B. Röck,[2,3] D. S. Aguado[2,3] and R. F. Peletier[6]

[1]*INAF-Osservatorio Astronomico di Capodimonte, sal. Moiariello 16, I-80131 Napoli, Italy*
[2]*Instituto de Astrofísica de Canarias, Calle Vía Láctea s/n, E-38205 La Laguna, Tenerife, Spain*
[3]*Departamento de Astrofísica, Universidad de La Laguna (ULL), E-38206 La Laguna, Tenerife, Spain*
[4]*Mullard Space Science Laboratory, University College London, Holmbury St Mary, Dorking, Surrey RH5 6NT, UK*
[5]*Astronomisches Rechen-Institut, Zentrum für Astronomie, Universität Heidelberg, Mönchhofstr. 12-14, D-69120 Heidelberg, Germany*
[6] *Kapteyn Astronomical Institute, University of Groningen, P. O. Box 800, NL-9700 AV Groningen, the Netherlands*

Accepted 2016 September 20. Received 2016 September 20; in original form 2016 May 31

ABSTRACT

We present a joint analysis of the four most prominent sodium-sensitive features (Na D, Na I λ8190Å, Na I λ1.14 μm, and Na I λ2.21 μm), in the optical and near-infrared spectral ranges, of two nearby, massive ($\sigma \sim 300$ km s^{-1}), early-type galaxies (named XSG1 and XSG2). Our analysis relies on deep Very Large Telescope/X-Shooter long-slit spectra, along with newly developed stellar population models, allowing for [Na/Fe] variations, up to ∼1.2 dex, over a wide range of age, total metallicity, and initial mass function (IMF) slope. The new models show that the response of the Na-dependent spectral indices to [Na/Fe] is stronger when the IMF is bottom heavier. For the first time, we are able to match all four Na features in the central regions of massive early-type galaxies finding an overabundance of [Na/Fe] in the range 0.5–0.7 dex *and* a bottom-heavy IMF. Therefore, individual abundance variations cannot be fully responsible for the trends of gravity-sensitive indices, strengthening the case towards a non-universal IMF. Given current limitations of theoretical atmosphere models, our [Na/Fe] estimates should be taken as upper limits. For XSG1, where line strengths are measured out to ∼0.8 R_e, the radial trend of [Na/Fe] is similar to [α/Fe] and [C/Fe], being constant out to ∼0.5 R_e, and decreasing by ∼0.2–0.3 dex at ∼0.8 R_e, without any clear correlation with local metallicity. Such a result seems to be in contrast to the predicted increase of Na nucleosynthetic yields from asymptotic giant branch stars and Type II supernovae. For XSG1, the Na-inferred IMF radial profile is consistent, within the errors, with that derived from TiO features and the Wing–Ford band presented in a recent paper.

Key words: galaxies: elliptical and lenticular, cD – galaxies: formation – galaxies: fundamental parameters – galaxies: stellar content.

1 INTRODUCTION

Although constraining the initial mass function (hereafter IMF) of unresolved stellar populations poses a number of difficult challenges, it has been possible to discern a significant variation of the low-mass end of the IMF in early-type galaxies (ETGs). Constraints on the IMF have been achieved on two fronts, namely via estimates of the stellar mass-to-light ratio (M/L) through dynamical (see, e.g. Cappellari et al. 2012, 2013) or lensing analyses (see, e.g. Treu et al. 2010; Leier et al. 2016); or via targeted spectral features sensitive to the presence of low-mass stars, which in effect constrain the relative contribution of dwarf versus giant stars (see, e.g. Cenarro et al. 2003; van Dokkum & Conroy 2010; Ferreras et al. 2013; La Barbera et al. 2013; Spiniello et al. 2014). These two approaches are affected by different systematics, but both agree in that the stellar populations found in the more massive ETGs appear to have formed from a (bottom-)heavier IMF than the standard one (see e.g. Kroupa 2001; Chabrier 2003). The more homogeneous populations typically found in massive ETGs simplify – to some degree – the analysis of the strong degeneracies found in the interpretation of gravity-sensitive spectral features. However, some issues of the analysis are not fully understood. These issues are mainly related to the sensitivity of the indices to non-solar abundance ratios, both as a general trend between the Fe-group and alpha-group elements

⋆E-mail: labarber@na.astro.it (FLB); vazdekis@iac.es (AV); i.ferreras@ucl.ac.uk (IF)

(measured as [Mg/Fe] or [α/Fe]), or as more specific variations in *individual* elements – described here as [X/Fe] – that affect the specific gravity-sensitive features under scrutiny.

The steps ahead in the interpretation of gravity-sensitive line strengths as a signature of a non-universal IMF involve a painstaking, detailed analysis of the inherent degeneracies of these indices. Although age and metallicity can be robustly taken into account by use of additional spectral indices, or by spectral fitting, the effect of [α/Fe] or, even more so, [X/Fe] is much harder to quantify, due to the lack of a fully consistent, extensive, library of stellar spectra (empirical or theoretical) covering a wide range of the parameter space. An empirically motivated approach is always preferred – given the complexity of the line strengths and the stellar populations under study. For instance, in La Barbera et al. (2013) it was possible to model the [α/Fe] dependence of the indices by use of stacks of Sloan Digital Sky Survey (SDSS) spectra selected at fixed velocity dispersion and [α/Fe]. Such an approach allowed us to discard, in an empirical way, the possibility that the trends found in gravity-sensitive indices were solely caused by variations in [α/Fe]. However, at the moment, it is not possible to base the analysis entirely on an empirical approach, and one has to resort to more uncertain stellar atmosphere calculations (see, e.g. Thomas, Maraston & Johansson 2011; Conroy & van Dokkum 2012a, hereafter CvD12a).

More empirical information is needed to advance in this field, and to improve theoretical models of stellar atmospheres. On this front, we turned towards a detailed analysis of the spectra of individual ETGs at very high signal-to-noise ratio (S/N), covering a wide spectral window. In this context, La Barbera et al. (2016, hereafter LB16) presented a high-quality spectrum of a massive ETG taken by the Very Large Telescope (VLT)/X-Shooter spectrograph, to explore the local (i.e. radial) variations in the IMF by use of TiO gravity-sensitive indices in the optical and near-infrared (NIR), as well as the Wing–Ford (FeH-dependent) band in the NIR. A combination of three TiO indices allowed us to break the degeneracies of individual line strengths, leading to a robust determination of a radial gradient in the IMF slope, being bottom-heavy in the central region, approaching the standard case at around an effective radius. This result is consistent with the previous studies (Martín-Navarro et al. 2015a). Surprisingly, the Wing–Ford index was not as strong as expected, and its radial variation was rather mild, apparently suggestive of no IMF change. However, one should note that each gravity-sensitive index depends on different intervals of the IMF stellar mass range. The Wing–Ford band is especially sensitive to the very low mass (VLM) end (i.e. the feature is only prominent in the coolest M-dwarfs). Therefore, this result is consistent with a scenario where the IMF of massive ETGs has an excess of low-mass stars (around a spectral type M0V, corresponding to a stellar mass of 0.5 $M_{\odot}$) but not of VLM stars (approximately below a spectral-type M4V, corresponding to 0.2 $M_{\odot}$), i.e. a tapering of the IMF functional form, similar to that for the Milky Way IMF. In this case, a single power law (also described as a unimodal IMF) is readily ruled out (La Barbera et al. 2016). Alternatively, one may consider that the Wing–Ford band is more strongly anticorrelated with [α/Fe] than the theoretical predictions, hampering its joint interpretation with the optical TiO indices.

The ultimate goal of the interpretation of gravity-sensitive spectral features is to determine the local property that drives the variations in the IMF. Various theoretical analyses propose an excess of low-mass stars through turbulent fragmentation in the environment of a strongly starbursting interstellar medium (see, e.g. Padoan & Nordlund 2002; Hopkins 2013; Chabrier, Hennebelle & Charlot 2014). On first principles, one could expect a significant variation in the IMF between a relatively quiet environment and a more extreme scenario – found in the cores of massive ETGs – where a substantial mass in stars ($\sim 10^{11}$ $M_{\odot}$) forms within a relatively short period of time (1–2 Gyr) and within a small volume (r < 1–2 kpc). Moreover, in order to match the observed properties of massive ETGs (most notably, their metallicity and α-enhancement), a time-dependent scenario is required, where a top-heavy phase, expected during the first stages of galaxy evolution, is followed by a bottom-heavy phase (Vazdekis et al. 1996, 1997; Weidner et al. 2013; Ferreras et al. 2015). A deeper understanding of the information encoded in gravity-sensitive spectral indices will allow us to determine the major driver of IMF variations. The large metallicity radial gradient found in (some) massive ETGs (see, e.g. La Barbera et al. 2012) is indicative of at least two different components: a massive, compact core, formed early, and an extended envelope, possibly made up of accreted material from mergers. This two-stage formation paradigm (e.g. Oser et al. 2010; Navarro-González et al. 2013) should also lead to two different stellar mass functions. Indeed, such a variation in the IMF was found in recent studies based on long-slit and integral field spectroscopy (Martín-Navarro et al. 2015a,c). The lack of an IMF radial gradient in a relic, compact, massive galaxy (Martín-Navarro et al. 2015b) was encouraging within this simple model. Furthermore, these spatially resolved studies allowed us to focus on the *local* drivers of IMF variations. Although the first results pointed to a significant correlation with central velocity dispersion (Ferreras et al. 2013, hereafter F13; La Barbera et al. 2013; Spiniello et al. 2014; La Barbera, Ferreras & Vazdekis 2015; Martín-Navarro et al. 2015a), the Calar Alto Legacy Integral Field Area Survey (CALIFA) revealed that metallicity, rather than *local* velocity dispersion, might be the primary driver of IMF variations (Martín-Navarro et al. 2015c). It is worth emphasizing here that the SDSS-based work is fully consistent with this interpretation, as a significant correlation is expected between metallicity and the fibre-integrated velocity dispersion measured in the SDSS spectra. However, the CALIFA results were mostly based on a single gravity-sensitive feature (TiO2), and more work is doubtlessly needed to disentangle the underlying degeneracies.

As a next step, we turn our focus towards the sodium-based indices. One of the key observables originally proposed to explore the low-mass end of the IMF in quiescent galaxies is the NIR Na I feature at 8190 Å (Spinrad & Taylor 1971). The strength of this feature in massive ETGs could be interpreted either as an excess of low-mass stars with respect to the Milky Way standard IMF; as a product of the expected supersolar [α/Fe]; or even as an overabundance in the individual elements that affect this index, most notably [Na/Fe]. A combination of indices, including the NaD feature in the optical, might allow us, in principle, to disentangle the effect of abundance variations from the presence of low-mass stars (Spiniello et al. 2012). However, such an analysis has been rather inconclusive so far, especially in light of recent results targeting specific (one or two; mostly optical) Na-sensitive features. Smith & Lucey (2013) found a giant elliptical galaxy with a lightweight IMF normalization – as constrained by strong lensing – in apparent contrast with its Na I λ8190 Å line as strong as in other high-σ ellipticals. Smith et al. (2015, hereafter SAL15) also concluded that state-of-the-art stellar population models struggle to reproduce the NIR Na I1.14 feature in most massive galaxies without breaking other constraints. Meneses-Goytia et al. (2015) also found that both their models and those of CvD12a are unable to reproduce the observed large Na I λ2.21 μm values of massive ETGs (see also Röck et al. in preparation). Recently, Zieleniewski et al. (2015) found a highly Na-enhanced population in the bulge of M31 – along with an Na-depleted

population in M32, still pointing to difficulties of the most recent stellar population models to match both the NaD and Na I λ8190 Å absorption lines. Furthermore, McConnell, Lu & Mann (2016) suggested large gradients in [Na/Fe] in the central regions of ETGs. These findings show that an in-depth analysis of sodium-dependent spectral features, in both the optical and NIR, is very much needed.

In this work, we perform, for the first time, a joint, radially extended, analysis of the four Na-sensitive spectral features, Na D, Na I λ8190 Å, Na I λ1.14 μm, and Na I λ2.21 μm (hereafter NaD, Na I8190, Na I1.14, and Na I2.21, respectively) in two massive ($\sigma \sim 300$ km s^{-1}) ETGs at redshift $z \sim 0.06$. The two targets, hereafter XSG1 and XSG2, have been selected from the Spheroid's Panchromatic Investigation in Different Environmental Regions (SPIDER) survey (La Barbera et al. 2010), more specifically from the subsample of 160 ETGs with $280 < \sigma < 320$ km s^{-1} defined by La Barbera et al. (2013, hereafter LB13). For both galaxies, we have gathered new, very deep, 'high' resolution ($R > 4000$), long-slit spectroscopy with the X-Shooter spectrograph at the European Southern Observatory–Very Large Telescope (ESO-VLT). Our main goal is to constrain, simultaneously, the effect of abundance ratios on Na lines (i.e. [α/Fe] and [Na/Fe]), as well as the slope of the stellar IMF in these galaxies. To model the effect of [Na/Fe], we rely on new stellar population models (named Na-MILES) developed specifically for the purpose of this work, extending previous models, covering the optical and NIR spectral ranges, from Vazdekis et al. (2012) and Röck et al. (2015). The effect of [α/Fe] is modelled with an empirical approach. The results presented in this work are intended to provide a calibration for the interpretation of Na-sensitive features in ETGs. To this effect, our newly developed Na-enhanced stellar population models are made publicly available.

The layout of the paper is as follows. In Section 2, we describe the data. The new stellar population models and the measurement of Na line strengths are described in Sections 3 and 4, respectively. Section 5 deals with the determination of stellar population parameters, such as [C/Fe] and [α/Fe], that are relevant for our analysis. The fitting methodology leading to the constraints on [Na/Fe], IMF slope, and the sensitivity of the Na indices to [Na/Fe] is presented in Section 6. Some important caveats are discussed in Section 8. The results are presented in Section 7, followed by a discussion and a summary in Sections 9 and 10, respectively. We include two appendices with detailed information about the effect of low-$T_{\rm eff}$ stars on the Na-MILES models (Appendix A) and on a comparison between CvD12a and our models (Appendix B).

2 DATA

The targets of this work are XSG1 (SDSS J142940.63+002159.0) and XSG2 (SDSS J002819.30−001446.7), two massive ($M_\star \sim 1$–2×10^{11} M$_\odot$; $\sigma \sim 300$ km s^{-1}) ETGs at redshift $z \sim 0.055\,74$ and $z \sim 0.060\,09$, respectively. Both galaxies are selected from the SPIDER survey (La Barbera et al. 2010), more specifically from the subsample of 160 ETGs with $280 < \sigma < 320$ km s^{-1} defined in LB13.

XSG1 has spherical morphology ($b/a \sim 0.9$, corresponding to an E0/E1 type), whose light distribution is well described by a de Vaucouleurs model, with an effective radius of $R_{\rm e} \sim 4.1$ arcsec (see LB16 for details). XSG2 has a flatter light distribution, with $b/a \sim 0.67$. Using the software 2DPHOT (La Barbera et al. 2008) to fit the SDSS r-band image of XSG2 with a two-dimensional, point spread function convolved, Sérsic model (as for XSG1, see LB16) gives a best-fitting Sérsic $n \sim 5.4$, and an effective radius of $R_{\rm e} \sim 5.4$ arcsec. Simard et al. (2011) report a total $R_{\rm e} \sim 4.2$ arcsec from the galaxy bulge+disc decomposition, while from SDSS, we retrieve a value of $R_{\rm e} \sim 4.1$ arcsec, more consistent with the total $R_{\rm e}$. Throughout this work,[1] for XSG2, we adopt an SDSS value of $R_{\rm e} \sim 4.1$ arcsec (i.e. the same value as for XSG1).

For both targets, we have obtained new, deep long-slit spectroscopy with the X-Shooter spectrograph at the ESO-VLT, on Cerro Paranal (Proposal IDs: 092.B-0378, 094.B-0747; PI: FLB). X-Shooter is a second-generation ESO-VLT instrument – a slit echelle spectrograph that covers a wide spectral range (3000–25 000 Å), at relatively high resolution (Vernet et al. 2011). The incoming beam is split into three independent arms (ultraviolet-blue, UVB: 3000–5900 Å; visible, VIS: 5300–10 200 Å; and near-infrared, NIR: 9800–25 000 Å), each one equipped with optimized optics, dispersive elements, and detectors, ensuring high sensitivity throughout the entire spectral range. Data for XSG1 (XSG2) were taken through 5 (10) observing blocks, each including two exposures on target, interspersed by 2 (1) sky exposures, with the same integration time as for the science target. This setup resulted into a total on-target exposure time of ∼1.7, 1.9, and 2.1 h, in the X-Shooter UVB, VIS, and NIR arms, respectively. For each arm, the data were pre-reduced using version 2.4.0 of the data-reduction pipeline (Modigliani et al. 2010), performing the subsequent reduction steps (i.e. flux calibration, sky subtraction, and telluric correction) with dedicated FORTRAN software developed by the authors. We refer the reader to LB16 for a detailed description of each reduction step (see also Schönebeck et al. 2014).

For this study, we use the six radially binned spectra of XSG1 analysed by LB16 (see their fig. 4), obtained by folding up data from opposite sides of the X-Shooter slit around the photometric centre of the galaxy. In order to minimize seeing effects, the innermost spectrum has a width of 1.3 arcsec (i.e. ±0.675 arcsec) around the photometric centre of the galaxy, corresponding to a factor of 1.5 times the mean seeing full width at half-maximum (FWHM) of the data. The bin size is increased adaptively outwards, in order to ensure a median S/N > 90 per Å in the optical spectral range (from 4800 to 5600 Å). The outermost bin for XSG1 reaches an average galactocentric distance of ∼0.8 $R_{\rm e}$. For XSG2, because of the lower[2] S/N, we did not extract spectra at different radii, producing only the central galaxy spectrum, extracted within an aperture of ±0.675 arcsec (i.e. ∼0.2 $R_{\rm e}$) around the galaxy photometric centre, i.e. the same aperture as for the innermost bin of XSG1. Thus, the present analysis is based on a total of seven radially binned spectra, six for XSG1 plus one for XSG2. The median S/N measured in the central bins reaches 320 and 220 per Å for XSG1 (see table 1 of LB16) and XSG2, respectively. The main properties of the seven binned spectra, including their galactocentric distance $R/R_{\rm e}$ and velocity dispersion (σ), are summarized in Table 1. The spectra of XSG1 are displayed, over the whole X-Shooter spectral range, in fig. 4 of LB16. For XSG1, the σ is measured as detailed in LB16, running the software PPXF (Cappellari & Emsellem 2004) on different spectral regions of the UVB and VIS X-Shooter arms ($\lambda\lambda$ = 4000–9000 Å), combining the corresponding probability distribution functions into final estimates. For the central spectrum of XSG2, the same approach gives $\sigma \sim 308 \pm 3$ km s^{-1}, in fair

[1] The value of $R_{\rm e}$ is only used to scale the galactocentric distance of spectra extracted in different radial bins. Hence, the adopted value of $R_{\rm e}$ does not affect at all our conclusions.

[2] The lower S/N ratio of the X-Shooter spectrum of XSG2 is due to the fainter mean surface brightness of the galaxy (with respect to XSG1), rather than a lower data quality.

Table 1. Main properties of the spectra used in this work. Columns 1 and 2 report the galaxy name and the galactocentric distance in units of R_e (see Section 2), respectively. Columns 3, 4, 5, 6, and 7 give velocity dispersion, age, total metallicity, [α/Fe], and [C/Fe] abundance ratios, respectively. Uncertainties are quoted at the 1σ level, and represent internal (statistical) errors. Note that age and metallicity are estimated through the fitting of Na lines and [MgFe]$'$ (see Section 6), while [α/Fe] and [C/Fe] are derived as described in Section 5.

Galaxy	R/R_e	σ (km s^{-1})	Age (Gyr)	[M/H] (dex)	[α/Fe] (dex)	[C/Fe] (dex)
(1)	(2)	(3)	(4)	(5)	(6)	(7)
XSG1	0	333 ± 3	10.3 ± 0.8	0.38 ± 0.02	0.38 ± 0.03	0.12 ± 0.02
XSG1	0.19	316 ± 3	10.3 ± 0.8	0.27 ± 0.03	0.38 ± 0.04	0.20 ± 0.02
XSG1	0.25	307 ± 3	10.3 ± 0.8	0.34 ± 0.04	0.41 ± 0.04	0.19 ± 0.03
XSG1	0.32	302 ± 3	10.3 ± 0.8	0.22 ± 0.03	0.35 ± 0.03	0.21 ± 0.03
XSG1	0.43	291 ± 3	10.3 ± 0.8	0.20 ± 0.03	0.35 ± 0.03	0.18 ± 0.03
XSG1	0.78	276 ± 3	10.3 ± 0.8	0.08 ± 0.03	0.19 ± 0.03	0.10 ± 0.02
XSG2	0	308 ± 3	7 ± 0.5	0.35 ± 0.02	0.27 ± 0.03	0.08 ± 0.03

agreement with the SDSS-DR7 estimate (292 ± 11 km s^{-1}), measured within the (larger) SDSS 1.5 arcsec radius fibre aperture.

3 STELLAR POPULATION MODELS

3.1 Extended-MILES models

We use the extended-MILES (Medium resolution INT Library of Empirical Spectra) stellar population models, covering the spectral range from 0.35 to 5 μm, at moderately high resolution. Such a wide wavelength baseline is achieved by combining single-age, single-metallicity, stellar population (SSP) spectra computed in various spectral ranges with our population synthesis code, in a self-consistent manner. The optical SSP spectra (Vazdekis et al. 2010; recently updated by Vazdekis et al. 2015, hereafter V15) are extended out to ∼0.9 μm, forming the so-called MIUSCAT SSPs (Vazdekis et al. 2012), and joined to those at redder wavelengths (Röck et al. 2015), as described in Röck et al. (2016). All these models are extensively based on empirical stellar libraries, namely MILES in the optical range (Sánchez-Blázquez et al. 2006), which together with Indo-US (Valdes et al. 2004) and CaT (Cenarro et al. 2001) are employed in the MIUSCAT models, and the Infrared Telescope Facility (IRTF) stellar library (Cushing, Rayner & Vacca 2005; Rayner et al. 2003) reaching out to 5 μm. The atmospheric parameters ($T_{\rm eff}$, log g, and [Fe/H]) of stars in the different libraries have been homogenized to match the calibration of MILES (Cenarro et al. 2007).

The models use two sets of scaled-solar theoretical isochrones, namely the ones of Pietrinferni et al. (2004, BaSTI) and Girardi et al. (2000, Padova00). In the case of BaSTI, non-canonical models are used, with the mass-loss efficiency of the Reimers law (Reimers 1977) set to $\eta = 0.4$. The BaSTI isochrones are supplemented with the stellar models of Cassisi et al. (2000), which allow us to cover the VLM regime down to 0.1 $M_\odot$. The temperatures of these low-mass stars are cooler than those of Padova00 (Vazdekis et al. 2012). Although the Padova00 isochrones are defined over a wide range of metallicities, the BaSTI models, supplemented by additional computations as described in V15, allow us to virtually double the number of metallicity bins. These two sets of isochrones include the thermally pulsing asymptotic giant branch (AGB) regime using simple synthetic prescriptions, providing a significantly smaller contribution for this evolutionary phase at intermediate-aged stellar populations in comparison to the models of Marigo et al. (2008) and Maraston (2005). Finally, there are differences between the BaSTI and Padova00 isochrones, described in detail in Cassisi et al. (2004), Pietrinferni et al. (2004), and V15. Throughout this paper, in order to allow for a direct comparison with results from our previous works (e.g. F13, LB13, and LB16), we rely on models based on the Padova00 isochrones.

To transform theoretical isochrone parameters into stellar fluxes, we use relations between colours and stellar parameters from empirical photometric libraries. We mainly use the metallicity-dependent relations of Alonso, Arribas & Martínez-Roger (1996) and Alonso, Arribas & Martínez-Roger (1999) for dwarfs and giants, respectively. We also use the metal-dependent bolometric corrections of Alonso, Arribas & Martínez-Roger (1995) and Alonso et al. (1999), for dwarfs and giants. We refer the interested reader to V15 for a complete description of the method and relevant references.

The synthetic spectrum of an SSP is obtained by integrating along the isochrone, following the approach described in V15, for the 'base' models (see below). The number of stars within a mass bin is given by the adopted IMF. The spectrum of a star – given by a choice of atmospheric parameters ($T_{\rm eff}$, log g, and [Fe/H]) – is obtained by applying a local interpolation scheme that takes into account the local density of reference spectra from the stellar library in this three-dimensional parametric space. The procedure is detailed in Vazdekis et al. (2003), and updated in V15 (see their appendix B). The interpolation scheme is optimized to overcome the limitations imposed by gaps and asymmetries in the distribution of reference stars in parameter space.

Models are constructed with four different IMF shapes, as described in Vazdekis et al. (2003) and V15. We use the multi-part power-law IMFs of Kroupa (2001), i.e. universal and revised, and two power-law IMFs, as defined in Vazdekis et al. (1996), i.e. unimodal (single segment) and bimodal. The lower and upper mass-cutoffs are set to 0.1 and 100 $M_\odot$, respectively. The unimodal and bimodal IMFs are defined by their logarithmic slopes, Γ and Γ_b, respectively. For reference, the Salpeter (1955) IMF is obtained when adopting a unimodal IMF with $\Gamma = 1.35$, whereas the Kroupa Universal IMF is closely approximated by a bimodal IMF with $\Gamma_b = 1.3$. Since the bimodal distribution consists of a power law at the high-mass end – smoothly tapered towards low masses – varying Γ_b changes the dwarf-to-giant ratio in the IMF through the normalization. While this approach is different with respect to a change of the IMF slopes at low mass and VLM [e.g. Conroy & van Dokkum (2012b, hereafter CvD12b)], this parametrization is good enough for our purposes, as in this work we do not aim at constraining the IMF shape in detail, but rather

to perform a comparison of observed and model Na line strengths, adopting an IMF functional form that is consistent with constraints from our previous work (LB16).

The (empirical) stellar libraries employed in our models unavoidably follow the characteristic abundance pattern imprinted by the star-formation history of our Galaxy. Since we use scaled-solar isochrones, and do not take into account the specific elemental abundance ratios of the stellar spectra, for which we simply assume [M/H] = [Fe/H], these models can be regarded as 'base' models (see V15). Base models are approximately self-consistent, and scaled-solar at around solar metallicity. In contrast, at low metallicity they lack consistency since we combine scaled-solar isochrones with α-enhanced stellar spectra. In V15, we computed self-consistent models in the optical range, which are either scaled-solar or α-enhanced, at all metallicities, with the aid of theoretical stellar spectra from Coelho et al. (2005, 2007). Hereafter, we refer to such models as α-MILES.[3] Briefly, to obtain an α-enhanced model in the high-metallicity regime, we compute a reference scaled-solar SSP spectrum using MILES and α-enhanced isochrones (from Pietrinferni et al. 2006), along with the corresponding scaled-solar and α-enhanced SSP spectrum based on the theoretical models of Coelho et al. (2005). The residual between these two SSP spectra defines the differential response due to the varying abundance ratio. Therefore, we apply this correction to the reference SSP MILES-based scaled-solar spectrum to obtain the desired α-enhanced data. For the purpose of this work, we only use α-MILES SSPs to compare the *empirically derived* constraints of ΔNaD/$\Delta[\alpha/\mathrm{Fe}]$ to model predictions (see Section 7.6). In general, the analysis of observed line strengths of ETGs is based on extended-MILES and Na-MILES (see Section 3.2) model predictions.

3.2 Na-MILES models

In this paper, we need to account for the effect of varying [Na/Fe]. Therefore, we modify the modelling approach followed in our previous papers. The most relevant differences with respect to V15 (where we compute α-enhanced, rather than Na-enhanced, models) are: (i) we fully rely on scaled-solar isochrones, and (ii) we apply theoretical differential corrections to [Na/Fe] overabundance, specifically computed for each individual stellar spectrum in our empirical library. Note that, in contrast, the α-enhanced models were based on differential corrections for *SSP spectra*. Furthermore, our [Na/Fe]-enhanced models are not restricted to the MILES spectral range, as we extend them out to the *K* band. Hereafter, we refer to these models as Na-MILES models.

Following Mészáros et al. (2012), we create synthetic stellar spectra for each of the 180 stars (from the IRTF library) used to build up our models. This choice is motivated by the fact that the stellar parameter coverage of this library is dense enough at around solar metallicity, leading to SSP models with good quality (see figs 5 and 8 in Röck et al. 2015). We obtained model atmospheres by interpolation of the ODFNEW[4] ATLAS9 models of Castelli & Kurucz (2004), using *kmod*.[5] The ODFNEW models are available for stars with effective temperatures higher than 3500 K. For cooler stars in the IRTF library, we adopt a fixed temperature of 3500 K. The models adopt a reference solar composition from Grevesse & Sauval (1998). Note that the main difference between the solar abundances of Grevesse & Sauval (1998) and more recent versions (e.g. Asplund et al. 2009) is related to carbon, nitrogen, and oxygen abundances, which are up to 0.2 dex higher than in the previous version. We scale the metal abundances according to [Fe/H] derived for spectra in the IRTF library, and use α-enhanced models (by 0.4 dex) for stars with [Fe/H] < -1.

The spectral synthesis was performed with the ASSϵT code (Koesterke, Allende Prieto & Lambert et al. 2008; Koesterke 2009), with line opacities compiled by Kurucz, with updates to atomic damping constants published by Barklem, Piskunov & O'Mara (2000), including transitions of H_2,CH, C_2, CN, CO, NH, OH, MgH, SiH, SiO, and TiO. The equation of state included the first 92 elements of the periodic table and 338 molecules (Tsuji 1973; with some updates), with partition functions from Irwin (1981). We did not include H_2O transitions in the line opacity calculations, since these become important for effective temperatures lower than about 3000 K, i.e. below our threshold of 3500 K (see above). We accounted for bound-free absorption from H, H^-, He I, and He II, and the first two ionization stages of C, N, O, Na, Mg, Al, Si, and Ca from the Opacity Project (see, e.g. Cunto et al. 1993) and Fe from the Iron Project (Nahar 1995; Bautista 1997). All models are computed under the assumption of local thermodynamical equilibrium or LTE. We refer the reader to Allende Prieto et al. (2008) for more details.

We compute synthetic stellar spectra for a range of [Na/Fe], from 0 to +1.2 dex in steps of 0.3 dex, covering the spectral range from 0.35 to 2.5 μm. We stress that model atmospheres were not computed for each [Na/Fe] abundance ratio, but were interpolated from the Castelli & Kurucz (2004) model grid, and therefore assuming a solar [Na/Fe] abundance ratio. The effect of variations in the Na abundance on the atmospheric structure is expected to be modest, since this element produces very limited opacity and only contributes free electrons in the outermost photospheric layers of the coolest stars (Mészáros et al. 2012), and therefore it was only considered at the spectral synthesis stage. The models are computed for a total metallicity of [M/H] > -0.25 dex, i.e. within the values found in massive ETGs. For a given value of [Na/Fe], we divide each Na-enhanced, theoretical, spectrum by its scaled-solar counterpart, to obtain the (multiplicative) differential response to [Na/Fe], which is applied to the empirical stellar spectrum. This procedure is applied to all the stars in the IRTF library. The correction for the other stellar libraries (MILES, Indo-US, and CaT), applies our local interpolation algorithm to obtain the corresponding Na responses. Note that for each library, the relevant parameters of the interpolator are adjusted to account for the maximum density of stars in that library (see Vazdekis et al. 2003). We smooth the theoretical stellar spectra, adjusting the effective resolution to match the instrumental configurations of the different stellar libraries. The spectral resolution is kept constant with wavelength (at FWHM = 2.5Å), for all libraries, except for the IRTF set, which is characterized by a constant $\sigma = 60$ km s^{-1}.

4 LINE STRENGTHS

In order to account for the effect of stellar population properties (i.e. age, metallicity, and abundance ratios) on Na-sensitive features, we measure for each spectrum a set of spectral indices: Mgb5177; Fe3 = (Fe4383 + Fe5270 + Fe5335)/3; C4668 (see Trager et al. 1998); the total metallicity indicator [MgFe]′(Thomas, Maraston & Bender 2003); as well as H β_o (the optimized H β index defined by Cervantes & Vazdekis 2009).

The wide wavelength baseline provided by X-Shooter allows us to simultaneously study all four Na-sensitive features with the

[3] The synthetic spectra of α-MILES models only cover the optical range ($\lambda \lesssim 7400$ Å).
[4] http://kurucz.harvard.edu/grids.html
[5] http://hebe.as.utexas.edu/stools

Table 2. Index definitions of the four Na-sensitive features. Wavelengths are quoted in the air system.

Index	Units	Blue pseudo-continuum (Å)	Central feature (Å)	Red pseudo-continuum (Å)	Reference
(1)	(2)	(3)	(4)	(5)	(6)
NaD	Å	5860.625–5875.625	5876.875–5909.375	5922.125–5948.125	Trager+98
Na I8190	Å	8143.000–8153.000	8180.000–8200.000	8233.000–8244.000	LB13
Na I1.14	Å	11 353.882–11 363.879	11 368.879–11 411.867	11 413.866–11 423.864	CvD12a+this work
Na I2.21	Å	22 012.000–22 039.000	22 041.000–22 099.000	22 100.000–22 156.000	CvD12a+this work

same instrument, namely the four doublets at 5890 and 5896 Å (NaD), at 8183 and 8195 Å (Na I8190), at 11381 and 11404 Å (Na I1.14), as well as at 22062 and 22090 Å (Na I2.21), respectively. For XSG1, the measurements are made in all six radial bins, except for Na I2.21, for which we omit the measurement in the outermost bin due to the lower S/N in the *K* band. Regarding our second target, XSG2 – for which we only use the central spectrum – we measure all four Na-sensitive features. Line strengths are computed according to the band definitions given in Table 2. The indices NaD and Na I8190 are defined in Trager et al. (1998)[6] and LB13, respectively, whereas Na I1.14 follows the definition of CvD12a, although shifting the blue pseudo-continuum bluewards by 3 Å, in order to avoid a residual from data reduction, mostly visible in the outermost spectra of XSG1, at $\lambda \sim 11\,366$ Å. Na I2.21 is based on the index defined by CvD12a, but decreasing (increasing) the lower (upper) limit of the blue (red) pseudo-continuum by 17(12) Å. This definition of Na I2.21 – featuring a wider region for the sidebands – reduces the statistical uncertainty on the derivation of the pseudo-continuum, yet avoiding contamination from sky residuals, without a significant change in the sensitivity to relevant parameters, such as line broadening, IMF, metallicity, and abundance ratios. This issue was verified with the aid of extended-MILES and CvD12a stellar population models. Note that at the redshift of our targets, all Na features (and in particular Na I8190) are not affected significantly by telluric absorption in the earth atmosphere. Moreover, the exquisite resolution provided by X-Shooter allows us to achieve a sub-per cent level accuracy in the removal of sky emission and telluric lines, as detailed in LB16.

All Na-sensitive indices as well as [MgFe]′ – which are fitted simultaneously (see Section 6) – are corrected[7] to a common velocity dispersion of $\sigma = 300$ km s^{-1}.

For each spectrum, the correction is done as follows. We compute the difference between the line strengths at the velocity dispersion of the data, and at the reference $\sigma = 300$ km s^{-1}, by use of the extended-MILES models. These differences are estimated for models with an (old) age of 11 Gyr (i.e. typical of XSG1, see LB16), at solar ([M/H] = 0) and supersolar ([M/H] = 0.22) metallicity, adopting two choices of bimodal IMF, namely a Kroupa-like distribution ($\Gamma_b = 1.3$) and a bottom-heavy IMF ($\Gamma_b = 3$). The median values of these differences are then subtracted off from the observed indices (both [MgFe]′and the Na-sensitive features). Note that for all Na-sensitive indices, the correction is largely model independent, differing by less than 0.015 Å among different models, i.e. significantly below the statistical error on line strengths. This is due to the fact that our data span a relatively narrow range in velocity dispersion, from ∼270 to ∼330 km s^{-1} (see Table 1). The corrected values of [MgFe]′ and Na indices are reported in Table 3. All the corrected line strengths are compared to predictions of models smoothed to the same velocity dispersion of 300 km s^{-1}.

5 ABUNDANCE RATIOS

Since the (optical) Na features are expected to be sensitive to [α/Fe] (see below), we estimate [α/Fe] for all spectra, relying on the scaled-solar [Z_{Mg}/Z_{Fe}] proxy (see LB13 and V15). This is defined as the difference between the total metallicity, at fixed age, derived from either Mgb5177 or Fe3. The proxy is converted[8] into [α/Fe] with the aid of the Thomas et al. (2011, hereafter TMJ11) stellar population models,[9] resulting into an accuracy (rms) of 0.025 dex in [α/Fe]. The values of [α/Fe] for XSG1 and XSG2 are reported in Table 1. Note that the derivation of [α/Fe] for XSG1 is the same as described in LB16 (see their fig. 7), where we also compared different methods to estimate [α/Fe], finding consistent results. XSG1 turns out to have an almost constant [α/Fe] profile, with a high value of [α/Fe] ∼ 0.4 dex in the centre, decreasing to ∼0.2 dex only in the outermost radial bin. We find for XSG2 [α/Fe] $\sim 0.275 \pm 0.03$. In addition to [α/Fe], we also estimate [C/Fe] (see LB16), as this is relevant to our discussion of abundance effects on the NIR Na-sensitive lines (see below). Due to the strong sensitivity of C4668 to carbon abundance (e.g. Tripicco & Bell 1995), we estimate [C/Fe] with this feature, fitting simultaneously Hβ_o, [MgFe]′, Mgb5177, Fe3, and C4668 with the extended-MILES models (see Section 3) adopting a Kroupa-like IMF. The fit is done by minimizing the rms scatter between the model and the observed line strengths with respect to [C/Fe] and [α/Fe] (see equation 1 of LB16), where the sensitivity of line strengths to [α/Fe] ([C/Fe]) is computed with α-MILES (CvD12a) models for a 13.5 Gyr old population at solar metallicity. As shown in LB16, the use of models with a bottom-heavy IMF only affects the estimate of [C/Fe], below 0.05 dex. Moreover, the estimate of [α/Fe] from this approach is fully consistent with that of the scaled-solar proxy. For XSG1, the [C/Fe] radial profile has a similar trend with respect to [α/Fe], being almost constant as a

[6] Note that, although we rely on the index definition of Trager et al. (1998), the indices are not measured in the Lick/IDS system, but at the effective resolution (including both velocity dispersion and instrumental resolution).

[7] Note that we prefer this approach, instead of smoothing all observed spectra to a common velocity dispersion (typically the maximum value measured in the sample), as it extracts the maximum amount of information from the data (see, e.g. LB13), avoiding any contamination of the relevant features by neighbouring sky residuals.

[8] Since the proxy is derived from Mg- and Fe-sensitive absorption lines, in practice, it measures [Mg/Fe], and the conversion to [α/Fe] assumes a given ratio among different alpha elements (such as, in TMJ11, or V15). This assumption does not affect our analysis, as we treat the sensitivity of Na-dependent lines to [α/Fe] in an empirical manner (i.e. the uncertainty on the conversion from [Mg/Fe] to [α/Fe] is absorbed by the α_{Na_j} coefficients; see Section 6).

[9] Note that, for the conversion of the proxy into [α/Fe], we use TMJ11, rather than α-MILES models, in order to allow for a direct comparison with our previous works (e.g. LB13; Martín-Navarro et al. 2015c). However, this choice does not affect our conclusions, as there is a tight correlation between [α/Fe] estimates based on α-MILES and TMJ11 models, as shown in fig. 30 of V15.

Table 3. Measured line strengths for the total metallicity indicator [MgFe]′, and for the four Na-sensitive features analysed in this work. All line strengths have been corrected to a velocity dispersion of 300 km s^{-1} (see Section 4). Error bars are quoted at the 1σ level.

Galaxy	R/R_e	[MgFe]′ (Å)	NaD (Å)	Na I 8190 (Å)	Na I 1.14 (Å)	Na I 2.21 (Å)
XSG1	0	3.59 ± 0.02	5.78 ± 0.03	1.08 ± 0.01	1.40 ± 0.05	2.25 ± 0.10
XSG1	0.19	3.33 ± 0.05	5.24 ± 0.07	0.96 ± 0.04	1.27 ± 0.08	1.81 ± 0.14
XSG1	0.25	3.38 ± 0.06	5.25 ± 0.08	0.93 ± 0.04	1.27 ± 0.10	2.05 ± 0.19
XSG1	0.32	3.25 ± 0.06	5.12 ± 0.08	0.88 ± 0.04	0.98 ± 0.11	1.92 ± 0.24
XSG1	0.43	3.24 ± 0.07	4.62 ± 0.09	0.85 ± 0.04	0.97 ± 0.15	1.89 ± 0.31
XSG1	0.78	3.09 ± 0.07	4.25 ± 0.10	0.76 ± 0.11	0.93 ± 0.22	
XSG2	0	3.49 ± 0.04	5.25 ± 0.05	0.92 ± 0.02	1.06 ± 0.10	2.11 ± 0.15

function of radius, with [C/Fe] $\sim$ 0.2 dex in all radial bins except for the innermost and outermost bins, where [C/Fe] $\sim$ 0.1 dex (see fig. 7 of LB16). The same approach gives [C/Fe] $\sim 0.08 \pm 0.03$ dex for the central spectrum of XSG2. Hence, XSG2 turns out to have significantly lower abundance ratios (both [α/Fe] and [C/Fe]) than XSG1 despite both galaxies having similar velocity dispersion. Moreover, the central spectra of XSG1 and XSG2 have fully consistent [α/Fe]/[C/Fe] ratios ($\sim$3.2 and $\sim$3.4, respectively). Note that in this work, the [C/Fe] estimates are used for discussion purposes only, and they do not enter the fitting procedure of Na-sensitive line strengths.

6 FITTING NA LINE STRENGTHS

6.1 The method

We fit the line strengths of all the available spectra simultaneously by minimizing the following equation:

$$\chi^2 = \sum_{i,j} (\mathrm{Na}^{\mathrm{obs}}_{j,i} - \mathrm{Na}^{\mathrm{mod}}_{j,i} - \alpha_{\mathrm{Na}_j} \cdot \mathrm{Na}^{\mathrm{mod}}_{j,i} \cdot [\alpha/\mathrm{Fe}]_i)^2 \cdot {\sigma_{j,i}}^{-2} + \sum_i ([\mathrm{MgFe}]'_{\mathrm{obs},i} - [\mathrm{MgFe}]'_{\mathrm{mod},i})^2 \cdot {\sigma_{[\mathrm{MgFe}]'_i}}^{-2} \quad (1)$$

where index i runs over the available spectra, index j refers to a given Na feature (with $\mathrm{Na}_j = \{\mathrm{NaD}, \mathrm{Na\,I\,8190}, \mathrm{Na\,I\,1.14}, \mathrm{Na\,I\,2.21}\}$), $\mathrm{Na}^{\mathrm{obs}}_{j,i}$ and $\mathrm{Na}^{\mathrm{mod}}_{j,i}$ are the observed and model Na-sensitive line strengths, $\sigma_{j,i}$ are the uncertainties on $\mathrm{Na}^{\mathrm{obs}}_{j,i}$, $[\alpha/\mathrm{Fe}]_i$ is the α-element abundance ratio for the ith spectrum, and α_{Na_j} the *normalized response* of the jth Na-sensitive index to [α/Fe], namely

$$\alpha_{\mathrm{Na}_j} = \frac{\delta(\mathrm{Na}_j)/\mathrm{Na}_j}{\delta[\alpha/\mathrm{Fe}]}. \quad (2)$$

The last term in equation (1) refers to the total metallicity indicator [MgFe]′, where $[\mathrm{MgFe}]'_{\mathrm{obs},i}$ and $[\mathrm{MgFe}]'_{\mathrm{mod},i}$ are the observed and model line strengths, respectively, and $\sigma_{[\mathrm{MgFe}]'_i}$ corresponds to the uncertainties on $[\mathrm{MgFe}]'_{\mathrm{obs},i}$. Note that $\mathrm{Na}^{\mathrm{obs}}_{j,i}$ is measured for the central spectrum of XSG2 as well as for all six radial bins of XSG1, except Na I 2.21 in the outermost bin. Hence, the χ^2 in equation (1) includes a total of 34 terms, i.e. $6 \times 4 - 1$ (XSG1) plus 4 (XSG2) constraints from Na features, along with 7 additional constraints from $[\mathrm{MgFe}]'_{\mathrm{obs},i}$. The free-fitting parameters in equation (1) are the $\{\alpha_{\mathrm{Na}_j}\}$'s, and – for each spectrum – its IMF slope, the $[\mathrm{Na}/\mathrm{Fe}]_i$, and $[\mathrm{M}/\mathrm{H}]_i$. This amounts to $4 + 7 + 7 + 7 = 25$ free-fitting parameters, plus two constrained best-fitting parameters for age (see Section 6.3 for details). Note also that while for each fit the values of $[\alpha/\mathrm{Fe}]_i$ are kept fixed in equation (1), the uncertainties on $[\alpha/\mathrm{Fe}]_i$ are correctly propagated to those on best-fitting parameters (see the end of Section 6.3). Moreover, at each step of the χ^2 minimization procedure, the values of $\sigma_{j,i}$ in equation (1) are updated,[10] in order to include also the error budget due to the uncertainties on $[\alpha/\mathrm{Fe}]_i$. All model line strengths in equation (1) are derived from the Na-MILES SSP models, and depend on age, metallicity, IMF, and [Na/Fe]. Note that stellar age is treated as a free-fitting parameter, assuming suitable priors/constraints, as detailed in Section 6.2. We prefer not to include any age indicator (i.e. Balmer lines) in equation (1) in order to avoid issues related to their sensitivity to the IMF,[11] as well as issues related to emission correction, dependence of Balmer lines on abundance ratios, and uncertainties on the absolute zero point of the age from different indicators (see also Section 6.3). Nevertheless, we confirm that the inclusion of Hβ_o in the analysis does not change significantly the results.

6.2 Assumptions

The terms $\alpha_{\mathrm{Na}_j} \cdot \mathrm{Na}^{\mathrm{mod}}_{j,i} \cdot [\alpha/\mathrm{Fe}]_i$ in equation (1) describe the response of the jth Na-sensitive feature to [α/Fe] for the ith spectrum, and account for the fact that Na-MILES models have not been computed for a varying [α/Fe]. More importantly, we aim to constrain the effect of [α/Fe] on an empirical basis, relying as much as possible on the data. Hence, in our approach, we treat the terms α_{Na_j} as free-fitting parameters. To this effect, we assume that the coefficients α_{Na_j} are constant, i.e. independent[12] of age, metallicity, and IMF, as well as any other stellar population properties (e.g. abundance ratios). This assumption is supported for NaD by the predictions of α-MILES SSP models (see V15), as shown in Table 4, where we report the values of $\alpha_{\mathrm{NaD}} = \frac{\delta(\mathrm{NaD})/\mathrm{NaD}}{\delta[\alpha/\mathrm{Fe}]}$ for models with different age, metallicity, and (bimodal) IMF slope. The derived α_{NaD} is roughly constant, with a median value of -0.83 dex^{-1}. Regarding other Na-sensitive features, Table 5 reports the values of α_{Na_j} for a CvD12a 13.5 Gyr SSP with solar metallicity, and a Chabrier IMF. Hereafter, we refer to these values as $\alpha_{\mathrm{Na}_j\,\mathrm{CvD}}$. Note that for the NaD index, $\alpha_{\mathrm{NaD,CvD}} \sim -0.6$ dex^{-1}, which is significantly lower than the value from the α-MILES models. This discrepancy is at least partly due to the fact that the CvD12a models are computed at fixed [Fe/H]

[10] In practice, this is done by adding in quadrature to the uncertainty on $\mathrm{Na}^{\mathrm{obs}}_{j,i}$, the term $\alpha_{\mathrm{Na}_j} \cdot \mathrm{Na}^{\mathrm{mod}}_{j,i} \cdot \sigma_{[\alpha/\mathrm{Fe}]_i}$, where $\sigma_{[\alpha/\mathrm{Fe}]_i}$ is the measurement error on $[\alpha/\mathrm{Fe}]_i$ (see Table 1).

[11] For instance, as discussed in V15, the dependence of Hβ_o on the IMF is model dependent: while the V15 models give a decrease with IMF slope, the CvD12a models show a slight increase.

[12] This assumption is adopted within the range of age and metallicity of our targets, i.e. old and metal-rich populations ($\gtrsim$8 Gyr; [M/H] $\gtrsim$ 0).

Table 4. Normalized response of NaD to [α/Fe] from α-MILES stellar population models, with varying IMF (column 1), age (column 2), and metallicity (column 3). Absolute (i.e. δNaD/δ[α/Fe]) and relative (i.e. δNaD/NaD/δ[α/Fe]) responses to [α/Fe] are listed in columns 4 and 5, respectively.

IMF	Age (Gyr)	[M/H] (dex)	$\frac{\delta NaD}{\delta[\alpha/Fe]}$ (Å dex^{-1})	$\frac{\delta NaD/NaD}{\delta[\alpha/Fe]}$ (dex^{-1})
(1)	(2)	(3)	(4)	(5)
$\Gamma_b = 1.30$	8	0.06	−2.44	−0.83
$\Gamma_b = 1.30$	14	0.06	−2.69	−0.81
$\Gamma_b = 3.30$	8	0.06	−3.30	−0.87
$\Gamma_b = 3.30$	14	0.06	−3.57	−0.85
$\Gamma = 2.30$	8	0.06	−3.04	−0.86
$\Gamma = 2.30$	14	0.06	−3.39	−0.85
$\Gamma_b = 1.30$	8	0.26	−2.91	−0.81
$\Gamma_b = 1.30$	14	0.26	−3.40	−0.83
$\Gamma_b = 3.30$	8	0.26	−3.72	−0.84
$\Gamma_b = 3.30$	14	0.26	−4.16	−0.84
$\Gamma = 2.30$	8	0.26	−3.40	−0.83
$\Gamma = 2.30$	14	0.26	−3.94	−0.84

Table 5. Normalized response of Na features to [α/Fe] (see equation 2) from CvD12a SSP models, with an age of 13.5 Gyr, solar metallicity, and a Chabrier IMF.

Index	$\alpha_{Na_j\,CvD}$ (dex^{-1})
(1)	(2)
NaD	−0.59
Na I8190	−0.83
Na I1.14	−0.07
Na I2.21	−0.20

metallicity (see V15 for details). Increasing [α/Fe] in the CvD12a models results in an increase in [M/H]. Since NaD increases with [M/H], the decrease of NaD with [α/Fe] is expected to be more pronounced at fixed [M/H] (i.e. α-MILES) than at fixed [Fe/H] (i.e. CvD12a). Note that according to the CvD12a models, one expects a very weak sensitivity of the NIR Na I1.14 and Na I2.21 indices to [α/Fe], making our assumption of constant α_{Na_j} for Na I1.14 and Na I2.21 more accurate. CvD12a predict a higher sensitivity to [α/Fe] of Na I8190 with respect to NaD. Although, we cannot test our assumption of a constant α_{Na_j} for Na I8190, we point out that under this assumption we are able to fit all Na features simultaneously for all available spectra. Moreover, the best-fitting value of α_{NaD} turns out to be remarkably consistent with that expected from the α-MILES models, as discussed in Section 7.

6.3 Fitting parameters and additional constraints

Our analysis relies on a total of 34 observed data points (see Section 6.1), and $4+7+7+7=25$ free-fitting parameters (i.e. $\{\alpha_{Na_j}\}$, the IMF slopes, $\{$ [Na/Fe]$_i\}$, and $\{$ [M/H]$_i\}$; see equation 1) plus two constrained best-fitting parameters related to age (see below). However, as described in Section 6.4, we also consider fits where the number of free parameters is significantly reduced, either by keeping fixed some of the $\{\alpha_{Na_j}\}$ or the IMF slopes fixed.[13] In these cases, we still find consistent results with respect to the general case. The minimization of equation (1) is performed by computing χ^2 over a grid of models with varying age, metallicity, IMF, and [Na/Fe], deriving the correction factors $\{\alpha_{Na_j}\}$ that minimize χ^2, for each position in the grid, based on a Levenberg–Marquardt algorithm. Note that while metallicity and IMF are free-fitting parameters for each spectra, the age is allowed to vary between 9 and 12 Gyr for XSG1, i.e. following the constraints obtained with different methods (see section 4.3 of LB16). In the case of XSG2, we assume a Gaussian constraint on the age of 8 ± 1.6 Gyr, inferred by comparing different methods (e.g. Hβ_o and full spectral fitting) as in XSG1 (see LB16). We impose as a further constraint that stellar age is the same for all spectra of XSG1, since this galaxy exhibits no significant age gradient (see LB16). These assumptions introduce two further constraints, i.e. the age of (all spectra) for XSG1 and the age of the central spectrum of XSG2. For completeness, we confirm that leaving the age parameter completely unconstrained for all spectra does not introduce significant changes. Note that there is a substantial uncertainty in the absolute determination of the age among different indicators (see, e.g. LB16). Thus, as mentioned in Section 6, we do not explicitly include any age-sensitive feature, such as Hβ, in equation (1), adopting instead the age constraints that account for differences among different methods. Regarding the $\{$ [α/Fe]$_i\}$ terms in equation (1), we keep them fixed to values computed from the optical lines (see Section 4 and Table 1). Uncertainties on best-fitting parameters in equation (1) are estimated from $N = 1000$ bootstrap iterations, where the fitting is repeated after shifting the observed line strengths and the values of $\{$ [α/Fe]$_i\}$ according to their uncertainties.

6.4 Fitting cases

We use equation (1) to constrain the relevant stellar population parameters, i.e. the relative response of the Na-sensitive features to [α/Fe] as well as the IMF slopes and [Na/Fe] abundance ratios for XSG1 and XSG2. In order to test the robustness of our results, the fitting is done for different cases, as summarized in Table 6. In all cases, we fit data for both galaxies simultaneously, while we consider different options. Note that in all figures, throughout this work, we apply the same colour coding for results derived from the same fitting scheme, as follows (see also Table 6).

A; *green*. We set the [α/Fe] sensitivity of the NIR Na features (Na I1.14 and Na I2.21) to zero based on the prediction from the CvD12a models (see Table 5 and Section 6). Additionally, we impose Gaussian constraints on the IMF slope of XSG1 for each radial bin. This is done by adding the term $\sum_i [\Gamma_{b,i} - \Gamma_{b,i,LB16}]^2/\sigma^2_{\Gamma_{b,i}}$ in equation (1), where $\Gamma_{b,\,i,\,LB16}$ and $\sigma_{\Gamma_{b,i}}$ are the IMF slope value derived for the ith radial bin of XSG1 from LB16 and its 1σ uncertainty, while $\Gamma_{b,\,i}$ is the IMF slope of the SSP model for which model line strengths ($Na^{mod}_{j,i}$ and $[MgFe]'_{mod,i}$) are computed at each step of the minimization procedure. Note that the IMF slope of XSG2 is treated as a free-fitting parameter.

B; *red*. Same as case (A), but without any constraint on the IMF for XSG1.

[13] Moreover, as mentioned in Section 9.1, we also get consistent results to those presented in this paper when including NaD and Na I8190 line strengths for the SDSS stacked with 300 km s^{-1} from LB13, in our fitting approach.

Table 6. Different fitting assumptions used in this paper, labelled by a letter (column 1), and shown in the figures with a colour and line type as given in columns 5 and 6, respectively. Among different cases, we vary the set of α_{Na_j} coefficients that are fitted to the data (column 2; see equation 1), the use of IMF constraints for XSG1 from LB16 (column 2), and the set of fitted Na-sensitive features (column 4).

Label (1)	α_{Na_j} (2)	IMF constraints for XSG1 (3)	Na features (4)	Colour (5)	Line type (6)
(A)	$\alpha_3 = 0, \alpha_4 = 0$	Yes	All	Green	Solid
(B)	$\alpha_3 = 0, \alpha_4 = 0$	No	All	Red	Dashed
(C)	$\alpha_3 = 0, \alpha_4 = 0$	Yes	No Na I2.21	Black	dot–dashed
(D)	All free	Yes	All	Blue	Dotted
(E)	All free	No	All	Magenta	Dash with three dots

C; *black*. Same as case (A), but without including Na I2.21 in the fit. This is motivated by the fact that the Na I2.21 line might be sensitive to other abundance ratios (e.g. [C/Fe], see Mármol-Queraltó et al. 2009; Röck et al. in preparation), besides [Na/Fe].

D; *blue*. All correction coefficients $\{\alpha_{\mathrm{Na}_j}\}$ are treated as free-fitting parameters, but IMF constraints are applied for XSG1.

E; *magenta*. Same as case (D), but without any constraint on the IMF of XSG1.

7 RESULTS

Fig. 1 shows the observed line strengths of Na-sensitive features in XSG1 (circles) and XSG2 (triangles), along with the best-fitting results from our SSP models that include a varying metallicity, (bimodal) IMF, and [Na/Fe]. All four Na-sensitive indices are shown as a function of the total metallicity indicator [MgFe]′. In a recent paper (LB16), we could rule out a single power-law (unimodal) functional form for the IMF in XSG1 on the basis of TiO and FeH gravity-sensitive indices. Hence, in this work we only consider a bimodal distribution. The black grids and solid dots in the figure show the response of the indices to [M/H] and IMF slope – derived from the extended-MILES models, i.e. at [Na/Fe] ~ 0 – while the grey grids correspond to (theoretical) models with [Na/Fe] $= +0.3$, $+0.6$, and $+0.9$ dex, respectively. Note that models with [Na/Fe] $= +1.2$ dex have also been computed (see Section 3), and used in the fitting procedure.[14] However, we do not show these high values in Fig. 1 to avoid overly increasing the range of index values along the vertical axes. The observed line strengths of NaD and Na I8190 (open circles and triangles) are corrected to $[\alpha/\mathrm{Fe}] = 0$ (filled circles and triangles), in order to allow for a direct comparison with the black and grey grids.[15] Note that the correction is negligible for Na I1.14 and Na I2.21 (see below). All model grids in the figure refer to the same (old) age of 11.2 Gyr, with line strengths given at a resolution of $\sigma = 300$ km s^{-1} (see Section 4).

[14] In practice, we allow [Na/Fe] to vary up to $+1.3$ dex, performing a linear (mild) extrapolation of model predictions above [Na/Fe] $= +1.2$ dex.

[15] The corrections are performed using best-fitting values of α_{NaD} and $\alpha_{\mathrm{NaI8190}}$ from method A (see Table 6). However, they are approximately independent of the fitting methodology as all methods give consistent estimates of α_{NaD} and $\alpha_{\mathrm{Na\,I8190}}$ (see Section 7.6).

7.1 Behaviour of the models

As seen in Fig. 1, Na-MILES models predict that *all* four Na-sensitive lines increase significantly with the IMF slope *and* [Na/Fe]. NaD is the most sensitive index to [Na/Fe], but it also increases significantly with the IMF slope, as already pointed out by LB13. Among the 'red' Na lines (Na I8190, Na I1.14, and Na I2.21), Na I1.14 is the most sensitive one to IMF variations followed by Na I8190 and Na I2.21. An important outcome is that the response of red Na lines to [Na/Fe] is strongly coupled with IMF variations. For a bottom-heavy distribution, the line strengths of red Na-sensitive features increase more with [Na/Fe] with respect to a Kroupa-like distribution. This trend effectively 'stretches' the grids in Fig. 1 along the IMF (vertical) axis for higher values of [Na/Fe]. This result is due to the fact that, for a given increase of [Na/Fe], the variation of Na-sensitive line strengths in cool dwarf stars is larger than that in other types of stars, making a bottom-heavy IMF boost up the effect of [Na/Fe] at the level of SSP model predictions. For Na I8190, a similar result was obtained by LB13 (see their fig. 15), who found that the response of Na I8190 to [Na/Fe], for a Salpeter IMF, is larger than that for a Kroupa-like distribution, based on an independent set of (fully theoretical) stellar population models. The behaviour of Na-MILES models is similar to that of CvD12a models, as both sets of models predict NaD to be very sensitive to [Na/Fe] (see light-green arrows in Fig. 1, corresponding to an increase of 0.3 dex in [Na/Fe] for CvD12a models) and Na I1.14 to be the line most sensitive to IMF (see fig. 12 of CvD12a). However, in contrast to CvD12a, who found that the sensitivity of Na I8190 and Na I1.14 to IMF is far larger than that to [Na/Fe], we find that the effect of [Na/Fe] is quite significant for *all* Na lines. Moreover, as one can see by comparing the size of light-green arrows in Fig. 1 to the offset between grids with [Na/Fe] ~ 0 (black) and [Na/Fe] $= +0.3$, our models predict a stronger increase with Na abundance than the CvD12a models. Despite these differences, as shown in Appendix B, our results remain essentially unchanged if one matches the IMF sensitivity of the Na line strengths of our models to those from CvD12a, in which case one derives mildly lower IMF slopes and higher [Na/Fe] abundances, in the central regions. We emphasize that while in the publicly available version of CvD12a models, the effect of [Na/Fe] is only computed at a given locus of parameter space (i.e. for a given age, metallicity, and for a Chabrier IMF), our new sets of models are the first ones providing SSP model predictions for different [Na/Fe] ratios, over a wide range of age, metallicity, and IMF slope. Another interesting aspect of Fig. 1 is that an increase of [Na/Fe] shifts the model grids towards lower values of [MgFe]′. In other words, [MgFe]′ decreases with [Na/Fe]. This is somewhat expected, as Na is a major electron donor, and thus it affects electron pressure and ionization balance in the stellar atmospheres. For instance, the line strength of the NIR calcium triplet lines decreases with [Na/Fe] (see CvD12a). Similarly, increasing [Na/Fe] makes the optical Fe and Mgb line strengths diminish, resulting in a lower [MgFe]′. This is relevant as in most stellar population studies, [MgFe]′ is adopted as a total metallicity indicator, and is assumed to be independent of abundance ratios. While this is approximately true for [α/Fe] (TMJ11; V15), this work shows that this is not the case for [Na/Fe]. Hence, for an Na-enhanced stellar population – as in the massive ETGs analysed in this work – one would tend to underestimate total metallicity when relying on scaled-solar SSP models. This explains why our best-fitting estimates of [M/H] for XSG1, based on Na-enhanced models (see Table 1), are larger, by about 0.1 dex, than those obtained with scaled-solar models (see fig. 5 of LB16).

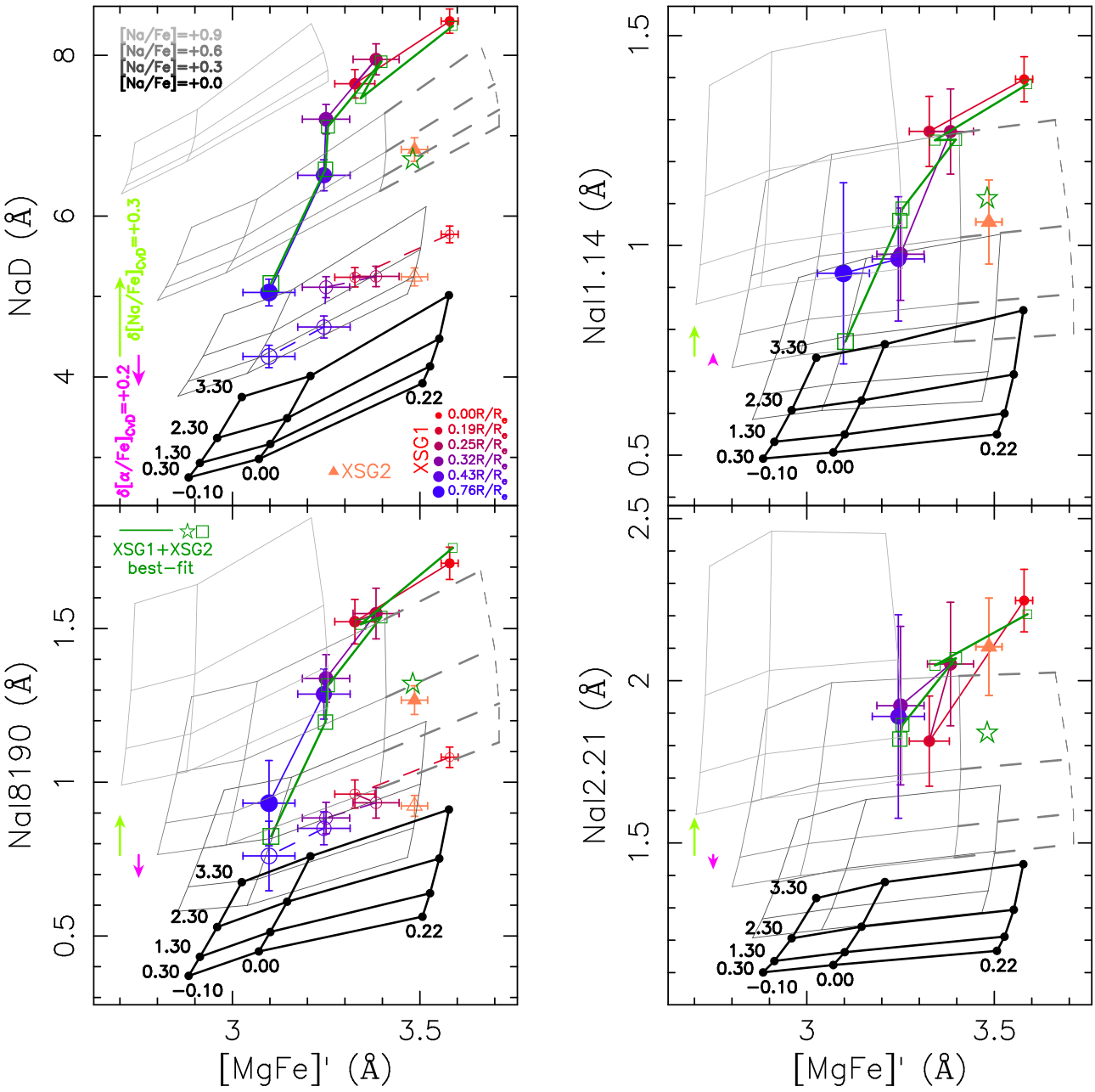

Figure 1. Line strengths of Na-sensitive features as a function of the total metallicity indicator [MgFe]′. Data points for XSG1 are plotted as circles, and colour-coded from red through blue, as a function of galactocentric distance (see labels in the lower-right corner of the top-left panel), while data points for XSG2 are shown as orange triangles. Symbol sizes increase with the galactocentric distance. In the panels for NaD and Na I8190, filled circles (connected by a solid line) and triangles plot line strengths corrected to $[\alpha/\mathrm{Fe}] = 0$, for XSG1 and XSG2, respectively, while open circles (connected by a dashed line) and triangles plot observed line strengths without any correction applied. The corrections are negligible for Na I1.14 and Na I2.21, as these indices are not sensitive to $[\alpha/\mathrm{Fe}]$. The black grids and black dots show predictions of extended-MILES SSP models with varying metallicity ($[\mathrm{M/H}] = -0.1$, 0, +0.22), bimodal IMF slopes ($\Gamma_\mathrm{b} = +0.3$, 1.30, 2.30, 3.30), and $[\mathrm{Na/Fe}] = 0$. Grey grids show predictions of Na-MILES models with $[\mathrm{Na/Fe}] = 0.3$, 0.6, and 0.9, respectively (see labels in the top-left corner). For reference, $\Gamma_\mathrm{b} \sim 1.3$ corresponds approximately to the case of a Kroupa IMF. All grids are computed for an age of 11.2 Gyr. For the grids with $[\mathrm{Na/Fe}] = +0.6$, we also show the linear extrapolation of the models, up to $[\mathrm{M/H}] = +0.4$, performed to match $[\mathrm{MgFe}]'$ for the innermost data points of XSG1 and XSG2 (see the text). In each panel, light green and magenta arrows show the effect of increasing $[\alpha/\mathrm{Fe}]$ ($[\mathrm{Na/Fe}]$) by +0.2 dex (+0.3 dex) on Na line strengths, according to CvD12a model predictions, computed for an age of 13.5 Gyr, solar metallicity, and a Chabrier IMF. Note that line strengths corrected to $[\alpha/\mathrm{Fe}] = 0$ (filled circles and triangles) can be directly compared to Na-MILES model predictions (i.e. black and grey grids). Green squares, connected by a solid line, and green stars are best-fitting results for XSG1 and XSG2, respectively, for our reference fitting approach (case A, see Section 6.4) where we constrain the IMF profile of XSG1 to be the same as that derived in our previous work (LB16). Note that we are able to match all Na-sensitive line strengths in both galaxies.

7.2 Comparison of data to model grids

Note that in Fig. 1 all data points remarkably lie above the model grids of the extended-MILES models (black grids with dots in the figure). Therefore, we can robustly confirm that no SSP model can match the observations with [Na/Fe] $\sim$ 0, regardless of the adopted IMF, even in the outermost radial bin of XSG1 where a solar metallicity is found (see LB16). Regarding NaD and Na I8190, whose line strengths are anticorrelated with [α/Fe] (see CvD12a; Spiniello, Trager & Koopmans 2015), the offset is significantly lower than in the NIR Na-sensitive lines (Na I1.14 and Na I2.21) for which the effect of [α/Fe] – according to the CvD12a models – is expected to be negligible. Qualitatively, the behaviour of the four Na-sensitive lines implies that, in addition to any possible IMF variation, [Na/Fe] has to be significantly enhanced in both XSG1, at all radii, and XSG2. In the optical lines, the effect of [Na/Fe] is (partly) counteracted by [α/Fe], reducing the mismatch from the [Na/Fe] = 0 grids. This can be seen by a comparison of the positions of the open circles and triangles in the left-hand panels of Fig. 1 – corresponding to the observed NaD and Na I8190 line strengths for XSG1 and XSG2, respectively – to the filled circles and triangles – that represent the line strengths after being corrected to [α/Fe] = 0, using the best-fitting values of α_{Na_j} (see equation 1), for method A (see Table 6). Note also that because the model [MgFe]$'$ decreases with [Na/Fe] (see above), in order to match models with [Na/Fe] $>$ 0 to the (high) values of [MgFe]$'$ for the innermost bins of XSG1 and XSG2, we need some extrapolation of the model grids to the high-metallicity regime, above the maximum value of [M/H] = 0.22 dex provided by MILES. To this effect, in the fitting procedure, all models are linearly extrapolated[16] up to [M/H] $\sim$ 0.4 dex. Extrapolated models are shown in Fig. 1 for models with [Na/Fe] = +0.6 dex. Because of the smooth shape of the grids in Fig. 1, the effect of extrapolation is mild, and affects only the analysis of the innermost spectra of our targets. Moreover, as discussed in Section 8, our conclusions do not change if we neglect the dependence of [MgFe]$'$ on [Na/Fe] (i.e. if we impose all grids in Fig. 1 to have the same [MgFe]$'$ as for [Na/Fe] = 0), in which case no extrapolation of the models is required.

7.3 Best-fitting line strengths

The dark green squares and stars in Fig. 1 show the best-fitting line strengths for XSG1 and XSG2, respectively, using the fiducial approach (case A, see Table 6), where we impose IMF constraints on XSG1 from LB16. Regarding NaD and Na I8190, the best-fitting line strengths are corrected to [α/Fe] = 0, and should be compared to the [α/Fe]-corrected data (filled circles and triangles for XSG1 and XSG2, respectively). The comparison shows a remarkable agreement between best-fitting and observed line strengths. This is shown more explicitly in Fig. 2, where we plot the difference of observed and best-fitting line strengths, normalized to their uncertainties, for all spectra and all features included in our fitting procedure. Our new Na-enhanced SSP models allow us to simultaneously match, at $\sim$1σ level, all four Na features in both galaxies. For Na I2.21, a mild difference (only at 1.5σ) is found for the second radial bin of XSG1, while a more significant difference is found for the central bin of XSG2, for which the best-fitting value is consistent with the observations only at the 1.8σ level (however,

[16] We also re-ran the fits by extrapolating the models up to [M/H] $\sim$ 0.6, finding no significant differences with respect to those reported throughout the paper.

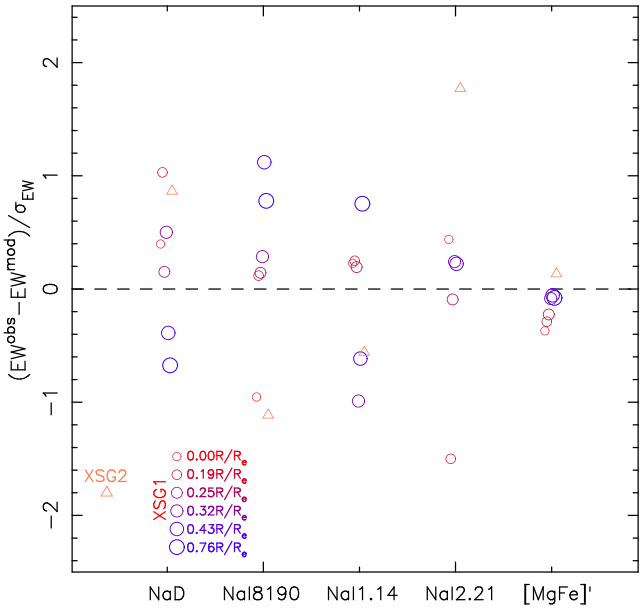

Figure 2. Differences between observed and best-fitting line strengths, normalized to their uncertainties, for all features and spectra included in our fitting procedures, using the fiducial approach (case A, see Table 6), where we impose IMF constraints on XSG1 from LB16. The horizontal dashed line marks the value of zero. Symbol types and colours for XSG1 and XSG2 are the same as in Fig. 1. Note that all features are fitted remarkably well, with typical differences $\lesssim$1σ.

note the comparatively large uncertainty on Na I2.21 for XSG2). Another possible explanation for this marginal discrepancy is that Na I2.21 is significantly affected by other abundance ratios. For instance, CvD12a models with supersolar [Si/Fe] cause an increase of Na I2.21, consistent with the fact that Si, an α element, is a significant absorber in the region where Na I2.21 is defined (Silva, Kuntschner & Lyubenova 2008). Moreover, Mármol-Queraltó et al. (2009) reported a significant correlation of Na I2.21 with the optical C4668 index in ETGs, implying a possible contribution of [C/Fe] to the index (Röck et al. in preparation). If this were the case, since XSG2 has lower [α/Fe] and [C/Fe] than XSG1 (see Table 1), we would expect a weaker Na I2.21 than the best-fitting solution, in contrast to the result shown in Figs 1 and 2. Furthermore, we are able to fit remarkably well the XSG1 data, including Na I2.21, at both the innermost and outermost radii. We notice that all the fitting scenarios (see Table 6) work equally well. To our knowledge, this is the first time that all the Na-sensitive line strengths in massive ETGs are matched simultaneously, in a consistent manner, from the optical to the NIR.

7.4 Best-fitting IMF slopes

Fig. 3 compares the best-fitting IMF slopes in XSG1 and XSG2 for the different fitting scenarios (see Section 6.4). Remarkably, when the IMF slopes in XSG1 are treated as free parameters, without any IMF constraint (red and magenta curves), the fit gives a bottom-heavy distribution in the innermost radial bin of this galaxy. In the outer regions, the values of Γ_b are fairly consistent with the profile derived by LB16 based on different IMF indicators (the cyan curve in the figure), although for the outermost radial bin, the Na-based IMF slope for XSG1 tends to be higher than that from LB16. Note that this does *not* imply an inconsistency among Na features and other IMF indicators (i.e. TiO and FeH; see LB16). In the

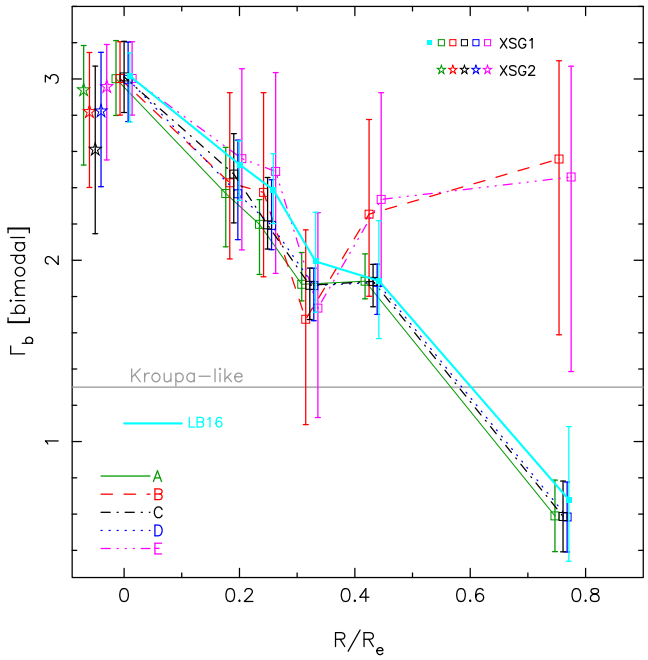

Figure 3. IMF slopes for different radial bins of XSG1 (squares) and the central spectrum of XSG2 (stars). The cyan, thick, solid profile corresponds to the radial slope of the IMF in XSG1 from LB16 that combined constraints from TiO features and the Wing–Ford band. Different fitting cases (see Section 6.4) are colour- and type-coded (see the lower-left corner in the figure), labelled as in Table 6. The error bars are shown at the 1σ level. Note that horizontal shifts have been applied among different fitting cases, for ease of visualization (the shift increases from case A through case E). The horizontal grey line corresponds to a Kroupa-like IMF. Note that in cases where no additional IMF constraints on XSG1 are applied (magenta and red curves), the best-fitting IMF slopes of XSG1, based on Na-sensitive features, are consistent with those derived by LB16, except for the outermost radial bin where, as shown by the large error bars, the IMF slope is poorly constrained (see the text).

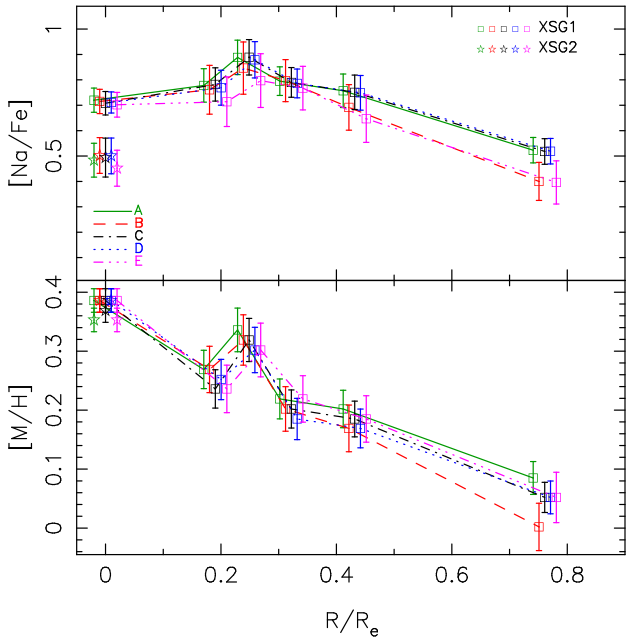

Figure 4. Best-fitting [Na/Fe] (upper) and [M/H] (lower panel) for different radial bins of XSG1 (squares) and the central spectrum of XSG2 (stars). The different fitting cases (see Section 6.4) are plotted with different colours and line types (Table 6). The error bars are shown at the 1σ level. Note that horizontal shifts have been applied among different fitting cases, to ease visualization. An [Na/Fe] as high as 0.7–0.8 dex is required to fit the data for XSG1, except for the outermost radial bin, where a lower [Na/Fe] value of 0.4–0.5 dex is found. The shape of the [Na/Fe] profile for XSG1 is remarkably similar to that of [C/Fe] and [α/Fe] (see fig. 7 of LB16), but shifted to higher values. XSG1 exhibits a negative metallicity gradient, typical of ETGs (see also LB16). The central spectrum of XSG2 is characterized by lower Na abundance than XSG1, with [Na/Fe] $= 0.5 \pm 0.08$ dex. Note that [Na/Fe] abundances should be taken as upper limits (see Section 8).

outermost radial bin, the uncertainty on IMF slope in XSG1 is too large to provide a significant constraint, being consistent at $\sim 1.2\sigma$ with either a bottom-heavy or a Kroupa-like ($\Gamma_b \sim 1.3$) slope. Hence, within error bars, the Na-based IMF trend for XSG1 is also consistent with the finding of LB16, i.e. a variation from the bottom-heavy slope in the centre to the Kroupa-like one beyond $\sim 0.5\,R_e$. In fact, when imposing additional IMF constraints on XSG1 (green, black, and blue curves), the inferred IMF profile is very consistent with that of LB16, with all Na features in the innermost and outermost bins being matched well, at $\sim 1\sigma$, from the best-fitting models (see Fig. 2). The large uncertainty on IMF slope in the outermost radial bin mostly reflects the large error bar on Na I1.14 (see Fig. 1), and the lack of Na I2.21. On the other hand, the [Na/Fe] is better constrained (see below), thanks to the smaller uncertainties on NaD (and Na I8190). Note also that, as discussed in Martín-Navarro et al. (2015a), for a 'light' IMF ($1 \lesssim \Gamma_b \lesssim 2$), it is far more difficult to obtain a fully consistent IMF determination among different indicators, as the IMF effect on spectral indices becomes subdominant with respect to that of other relevant parameters (e.g. abundance ratios).

For what concerns XSG2, our analysis also points to a bottom-heavy distribution in the central region. However, in this case, the data are also consistent with a lighter distribution, with $\Gamma_b \sim 2.2$, or even lower (see the black star with error bar in Fig. 3).

7.5 Best-fitting [Na/Fe]

The upper panel of Fig. 4 shows the radial profile of [Na/Fe] in XSG1, and the central value of XSG2, while the bottom panel of this figure shows the best-fitting values of [M/H] for all spectra. Lines with different colours and types correspond to the different fitting schemes considered. All methods produce a flat radial trend of [Na/Fe] in XSG1, with, on average, a high value of ∼0.7–0.8 dex, and a somewhat lower value of ∼0.4–0.5 dex in the outermost radial bin. We also infer a high [Na/Fe] abundance ratio in XSG2 (∼0.5 dex), albeit significantly lower than the central value for XSG1. Note that among all the fitting methods, the best-fitting [Na/Fe] is consistent within the 1σ confidence level. The high value of [Na/Fe] in XSG1 is consistent with the fact that this galaxy is the one with the highest NaD line strength among the SDSS ETGs with velocity dispersion $\sigma \sim 300$ km s^{-1} analysed by LB13 (i.e. NaD ∼ 5.5 ± 0.15 Å within the SDSS fibre aperture). On the other hand, XSG2 has a significantly lower strength (NaD $\sim 4.85 \pm 0.2$ Å) consistent with the lower [Na/Fe] inferred here (see Table 3). Together with Fig. 3, Fig. 4 shows that in order to fit all Na-sensitive features consistently in XSG1 and XSG2, we need both a bottom-heavy IMF and [Na/Fe] overabundance. Indeed, for Na I8190, Na I1.14, and Na I2.21, a bottom-heavy distribution works as a catalyst to the response with [Na/Fe], boosting the line strengths significantly with respect to a standard IMF. Note that for a Kroupa-like IMF, the central values of Na I1.14 and Na I2.21 in XSG1 would imply [Na/Fe] $\gtrsim 1.2$ dex. This seems rather unrealistic, even considering

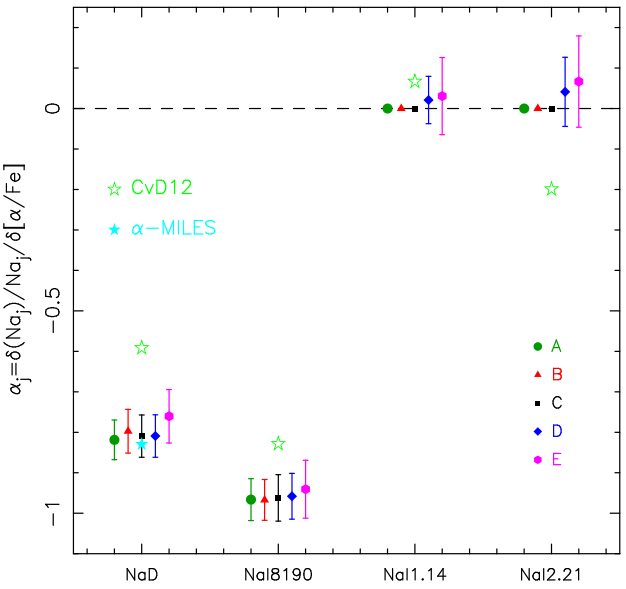

Figure 5. Best-fitting values of the responses of Na features, $\{\alpha_{\mathrm{Na}_j}\}$, to [$\alpha$/Fe] (see equations 1 and 2). From left to right, we plot values of α_{Na_j} for NaD, Na I8190, Na I1.14, and Na I2.21, respectively. The different fitting cases (see Section 6.4) are colour (Table 6) and symbol coded (see the legend in the figure). The error bars are shown at the 1σ level. Note that no error bars are shown when the α_{Na_j} coefficients are kept fixed in the fitting. Horizontal shifts have been applied among different fitting cases, for displaying reasons, with shifts increasing from case A through E. For comparison, light green open stars show the values of α_{Na_j} predicted for the CvD12a SSP models with an age of 13.5 Gyr, solar metallicity, and a Chabrier IMF. Note that the CvD12a models are computed at fixed [Fe/H], rather than total metallicity (as in the extended-MILES models), complicating the comparison to our results, especially for NaD and Na I8190 (which have a stronger dependence on [M/H]). Remarkably, our best-fitting results for NaD are fully consistent with (independent) model predictions based on α-MILES models (cyan filled star; see the text and Table 4), taking the effect of [α/Fe] explicitly into account (at fixed [M/H]).

that [Na/Fe] can be as high as 0.8 dex in the globular clusters (GCs) of M31 (Colucci, Bernstein & Cohen 2014). Such a high sodium abundance would imply NaD strengths around 10–11 Å (based on our models) – far larger than the observed values – as well as extremely high metallicities, above 0.5 dex (in order to match the observed [MgFe]$'$ in the innermost radial bin). As shown in Figs 3 and 4, the simultaneous fitting of the Na-sensitive line strengths rules out this kind of scenario.

7.6 Empirical response of Na-sensitive features to [α/Fe]

Fig. 5 shows the best-fitting values of α_{Na_j}, for all four Na-sensitive lines, comparing them to the predictions from the CvD12a models (green stars) and the α-MILES models (only for NaD, cyan star; see Section 4 and Table 4). We remark that the comparison to the CvD12a models should be taken with caution, as these models are computed at fixed [Fe/H], whereas the Na-MILES, α-MILES, and extended-MILES models are all computed at fixed total metallicity, [M/H]. Interestingly, we find that the response of Na I1.14 and Na I2.21 to [α/Fe] is consistent with zero (see the magenta and blue circles, with error bars, in the figure). In the case of Na I1.14, this result is fully consistent with the CvD12a prediction, while for Na I2.21, the CvD12a models predict a slight anticorrelation with [α/Fe] (i.e. $\alpha_{\mathrm{Na\,I2.21}} \sim -0.2$), not confirmed by our analysis. For NaD and Na I8190, the CvD12a models lie systematically above the best-fitting values of $\alpha_{\mathrm{Na\,I1.14}}$ and $\alpha_{\mathrm{Na\,I2.21}}$. Qualitatively, this is expected, as both NaD and Na I8190 increase with *total metallicity*, and thus the [α/Fe] dependence is expected to be stronger at fixed [M/H] than at fixed [Fe/H] (see Section 6.2). Note that the coefficient α_{NaD} from the α-MILES models (the cyan star) is more negative than the corresponding one from the CvD12a models. One of the most remarkable results of this study is that the best-fitting value of α_{NaD} is *fully consistent*, within the errors, with the prediction of the α-MILES models. This result is far from trivial, as in the α-MILES models the effect of [α/Fe] is taken into account by use of the recent [Mg/Fe] determinations of MILES stars, along with theoretical corrections, whereas in this work, we fully rely on theoretical corrections for the effect of [Na/Fe], constraining, empirically, the effect of [α/Fe]. The fact that the best-fitting and α-MILES values of α_{NaD} are fully consistent proves the internal consistency of our modelling approach and the robustness of these results.

8 CAVEATS

An important aspect of the present analysis is that absolute values of [Na/Fe], as inferred from Na-MILES model predictions (see the upper panel of Fig. 4), should be taken as upper limits. Our model line strengths depend mildly on how one treats the response of the spectra of cool stars to [Na/Fe]. In our reference modelling approach (see Section 3.2), we assume that the relative response of stellar spectra to [Na/Fe] in stars with an effective temperature of $T_{\mathrm{eff}} \lesssim 3500$ K – for which synthetic stellar atmosphere models are not available – is the same as for stars with 3500 K (see Section 3). In Appendix A, we compare our reference model predictions (Fig. 1) to those from a linear extrapolation of the response to [Na/Fe] for stars cooler than 3500 K. The extrapolation does not affect significantly NaD and Na I8190, while Na I1.14 and Na I2.21 increase slightly ($\lesssim$8 per cent), mostly at high metallicity and for a bottom-heavy IMF. As a result, the use of temperature-extrapolated models results in mildly lower values of [Na/Fe] (by $\sim$0.1 dex) with respect to the results shown in the upper panel of Fig. 4. Therefore, none of the conclusions in this work are affected. More importantly, one should note that our stellar atmosphere models are based on LTE. For a solar-like star, LTE predicts weaker lines (Allende Prieto, Hubeny & Lambert 2003), needing corrections that, for the strongest and saturated lines, can be as high as an equivalent change in the abundance of $\sim$0.5 dex. For a lower temperature star (with $T_{\mathrm{eff}} \sim 4000$ K), more relevant for models having old ages (such as those of our sample of ETGs), we may expect non-LTE (NLTE) corrections in the range of 0.1–0.2 dex (based on fig. 4 of Lind et al. 2011). Hence, we may expect that our LTE-based models predict weaker Na I lines, leading to high inferred values of [Na/Fe], an issue that has to be addressed with future model developments. We emphasize that our analysis matches NaD, Na I8190, Na I1.14, and Na I2.21, simultaneously, suggesting that the NLTE case will likely affect all four indices in a similar way. If this interpretation holds and NLTE corrections were significant, the Na-enhanced model grids in Fig. 1 should be affected in two ways: (i) the values of [Na/Fe] ($=\{0.3, 0.6, 0.9\}$) for the grids should be lower than those reported in the figure; and (ii) as a consequence, the Na-enhanced grids would not shift so much towards the lower values of [MgFe]$'$, with respect to Fig. 1. In order to test how the second effect would impact our results, we re-ran the fitting case B (see Section 6.4) by neglecting the dependence of [MgFe]$'$ on [Na/Fe] (i.e. we assume [MgFe]$'$ values from the extended-MILES models, with [Na/Fe] = 0). Note that in this case, no extrapolation of the grids in Fig. 1 is required,

as the high values of [MgFe]′ for the central spectra of XSG1 and XSG2 can be roughly matched with the highest metallicity ([M/H] = +0.22) of extended-MILES models. We found that neglecting the dependence of [MgFe]′ on [Na/Fe] produces an IMF profile as well as α_{Na_j} values (see Section 7.6) that are fully consistent with those for case B (Figs 3 and 5), whereas the [Na/Fe] estimates would (virtually) be ∼0.15 dex higher than those in Fig. 1, hence not changing our conclusions significantly.

9 DISCUSSION

9.1 Na abundance ratios in massive ETGs

Based on independent stellar population models, Conroy, Graves & van Dokkum (2014) and Worthey, Tang & Baitian (2014) reported [Na/Fe] ∼ 0.4 dex, in a set of stacked ETG spectra from SDSS, over a range of velocity dispersion $\sigma \sim 260$–300 km s^{-1}. These values agree well with the estimate for XSG2: [Na/Fe] = 0.5 ± 0.08 dex. Worthey et al. (2014) report values of [Na/Fe] as high as ∼0.55 dex for individual Virgo cluster galaxies, while CvD12b find [Na/Fe] ratios as high as ∼0.8 dex in some ETGs, and even 1 dex in the bulge of M31. Note that XSG1 gives a similarly high value: [Na/Fe] ∼ 0.7 dex. Therefore, XSG1 features an 'extreme' sodium abundance, as confirmed by its NaD line strength, the highest among SDSS galaxies with similar velocity dispersion (see Section 7). We have also modified our approach to fit the XSG1 and XSG2 line strengths simultaneously to NaD and Na I8190 data for the 300 km s^{-1} SDSS stacked spectrum of ETGs from LB13. In this case, we are able to match both the X-Shooter and SDSS data simultaneously, finding an abundance of [Na/Fe] = 0.42 ± 0.05 dex, fully consistent with Conroy et al. (2014), and an IMF slope of $\Gamma_{\mathrm{b}} = 2.7 \pm 0.4$ for the SDSS stack, consistent with the IMF–σ relation derived by LB13 (see their fig. 12).

It is important to emphasize that any estimate of [Na/Fe] should be actually taken as an upper limit. Note that we can compute the theoretical response of stellar spectra to [Na/Fe] only for stars hotter than 3500 K (see Section 3.2). As discussed in Appendix A, a linear extrapolation of Na responses to cooler temperatures would likely lead to lower [Na/Fe] estimates, by about 0.1 dex. Moreover, as already noticed by CvD12b, atomic NaI transitions in the atmospheres of late-type stars are prone to substantial departures from LTE (Bruls, Rutten & Shchukina 1992; Gehren et al. 2006; Andrievsky al. 2007; Lind et al. 2011). In a Sun-like star, LTE calculations predict weaker lines (Allende Prieto et al. 2003) requiring corrections for the strongest lines, which can be as high as an effective change in the abundance of ∼0.5 dex. For a lower temperature star (with $T_{\mathrm{eff}} \sim 4000$ K), more relevant for models having old ages (as those of our sample of ETGs), we may expect NLTE corrections in the range of 0.1–0.2 dex (based on fig. 4 of Lind et al. 2011). Hence, we may expect that NLTE models could enhance the predicted absorption in Na indices, resulting in lower inferred values of [Na/Fe]. However, note that our LTE-based methodology can match NaD, Na I8190, Na I1.14, and Na I2.21, simultaneously, suggesting that NLTE corrections should be approximately the same for all four Na lines – an important aspect to test with future models. We emphasize that although we have introduced four free-fitting parameters to match the four Na lines (the α_{Na_j} constants; see equation 1), in practice, the values of α_{NaD}, $\alpha_{\mathrm{Na\,I1.14}}$ and $\alpha_{\mathrm{Na\,I2.21}}$ are fully consistent with those of α-MILES and CvD12a models. Effectively, we are able to fit the four Na-sensitive line strengths of the seven X-Shooter spectra – spanning a range of age, metallicity, and [α/Fe] – based on only one 'extra' free-fitting parameter (i.e. the $\alpha_{\mathrm{Na\,I8190}}$).

We notice that previous works constrained [Na/Fe] only with one, or at most two, Na-sensitive lines (NaD and Na I8190). For instance, CvD12b mostly rely on the Na I8190 line, constraining sodium abundance from its indirect effect on the spectrum, due to its influence on the free electron abundance in the stellar atmospheres. One important concern when using NaD is the effect of dust absorption (Sparks, Carollo & Macchetto 1997; Jeong et al. 2013), either a foreground component from our Galaxy (not the case given the redshift of our sources) or intrinsic to the targeted systems. However, the observed NaD does not depend significantly on $E(B-V)$ for massive ETGs in SDSS (LB13). Moreover, the effect of reddening should be more prominent in low-σ (hence younger) galaxies, whereas the inferred [Na/Fe] is found to *increase* with velocity dispersion (based on NaD; Conroy et al. 2014). Our work suggests a negligible role of dust absorption on NaD, as this feature is matched simultaneously to the NIR lines, where the effect of reddening is completely negligible. This is not surprising, considering that our targets have been intentionally selected from the pool of SDSS massive galaxies with low internal extinction (see LB13).

Notwithstanding the above issues, a high sodium overabundance in massive ETGs is a plausible scenario. However, an explanation is not clear. High values of [Na/Fe] have been measured in individual stars in GCs. For instance, Colucci et al. (2014) found [Na/Fe] ∼ 0.8 dex in M31 GCs. In GCs, high Na abundances are usually associated with low oxygen abundances, i.e. the well-known Na–O anticorrelation (e.g. Carretta et al. 2009). While one might be tempted to relate this trend in GCs to the high [Na/Fe] in massive ETGs, the observations do not support the existence of such anticorrelation in galaxies. For instance, both [Na/Fe] and [O/Fe] are found to increase with galaxy velocity dispersion (Conroy et al. 2014).

Regarding the chemical enrichment aspect of the problem, sodium can be synthesized both in massive (>8 $\mathrm{M}_{\odot}$) and intermediate-mass ($3 < M/\mathrm{M}_{\odot} < 8$) stars. The former produces Na during the hydrogen burning process (via the $^{22}\mathrm{Ne}(p,\gamma)^{23}\mathrm{Na}$ reaction) and also via carbon burning (where ^{23}Na is an intermediate product of the full $^{12}\mathrm{C} + {}^{12}\mathrm{C}$ chain). At solar metallicity, the stellar models of Chieffi & Limongi (2004) predict a sodium enrichment by a factor between a few tens and $\sim 10^3$ in the stellar mass range 13–35 $\mathrm{M}_{\odot}$. The synthesized sodium is later ejected into the interstellar medium through stellar winds and mass loss during the Wolf–Rayet phase, and subsequently via supernova (SN) explosion. Nucleosynthetic yields of Na from this channel are expected to increase significantly with metallicity, even more than for other odd-Z elements (e.g. Al; see Kobayashi et al. 2006). Intermediate-mass stars, more massive than ∼3 $\mathrm{M}_{\odot}$, contribute to the synthesis of Na in their AGB phase, where Na is produced via hot-bottom burning (following the $^{22}\mathrm{Ne}(p,\gamma)^{23}\mathrm{Na}$ reaction) in their convective envelope, and during their interpulse period. The stellar models computed by Ventura et al. (2013) show that the amount of Na produced by massive AGB stars strongly increases with increasing metallicity (up to the maximum value probed, i.e. $\sim 2\,\mathrm{Z}_{\odot}$) at all stellar masses between 3 and 8 $\mathrm{M}_{\odot}$. At solar metallicity, the Na enrichment achieved by massive AGB stars is a factor of ≤2. The freshly synthesized Na is released to the interstellar medium via the heavy mass loss experienced by these stars during their AGB phase and at the AGB tip. The comparison of Na yields computed for massive stars by Chieffi & Limongi (2004) with those calculated for massive AGB stars by Ventura et al. (2013) indicates that massive stars are the dominant channel for Na enrichment in galaxies. Nevertheless, a bottom-heavy IMF, as measured in XSG1 and XSG2,

might make the contribution of massive AGB stars more relevant. Note that for both formation channels (SNe and AGB production), one would expect a correlation of [Na/Fe] with metallicity, which we do not see, as a function of galactocentric distance. [Na/Fe] does not show any significant radial variation in the inner region of this galaxy (out to $\sim$0.5 R_e), in contrast to the change in metallicity ($\sim$0.2 dex; see the lower panel of Fig. 4) over the same radial range. Moreover, as mentioned in Section 7, the radial behaviour of [Na/Fe] in XSG1 (Fig. 4) is very similar to [α/Fe] and [C/Fe] (see fig. 7 of LB16). A possible explanation is that Na yields do rapidly reach a saturation at supersolar metallicities, possibly giving no correlation of [Na/Fe] with [M/H] in this regime. Alternatively, under a time-dependent IMF scenario (Vazdekis et al. 1996, 1997; Weidner et al. 2013; Ferreras et al. 2015), both Mg and Na might have been produced during the early, low-metallicity, top-heavy phase of galaxy formation. In order to test these scenarios, a more detailed analysis of how Na is produced in massive and AGB stars, at different metallicities, would be required.

9.2 The IMF of ETGs from Na lines

Previous studies have claimed that in order to explain the optical Na-sensitive lines of massive ETGs – in particular NaD and Na I8190 – high sodium enhancement and a dwarf-rich IMF might be required (Spiniello et al. 2012). This work shows, for the first time in a quantitative manner, that the combination of *both* sodium enhancement and a dwarf-rich IMF is crucial to explain the optical *and* NIR Na-sensitive lines.

The interpretation of NIR Na lines has been hampered by a significant mismatch between the observations and the models. SAL15 have recently shown that state-of-the-art (CvD12a) stellar population models struggle to reproduce the NIR Na I1.14 in most massive galaxies. For a stacked spectrum of ETGs with $<\sigma> \approx 300$ km s^{-1}, SAL15 found that the observed line strength of Na I1.14 is significantly stronger than that of a best-fitting model based on full spectral fitting. The mismatch is $\sim$15 per cent, as shown by the blue cross and a red circle in fig. 3 of SAL15. Our results seem to reduce this discrepancy; as for a bottom-heavy distribution (typical of the average population of massive ETGs), say $\Gamma_b = 3.3$, and for 'high' [Na/Fe] ($\sim$0.6 dex), our models predict Na I1.14 strengths that are 15 per cent higher (i.e. similar to the offset in fig. 3 of SAL15) than what one would get when evaluating the impact of [Na/Fe] on Na I1.14 for a Kroupa-like IMF. Note that this argument does not solve the issue of an high Na I1.14 for some massive galaxies with an IMF normalization close to Kroupa, as found by SAL15. However, it could help reduce the tension. In fact, even for a relatively 'light' IMF, such as a bimodal IMF with $\Gamma_b = 2.3$ (corresponding to a mass-excess parameter, $(M/L)/(M/L)_{Kroupa} \sim 1.3$, i.e. an M/L only slightly above that for a Kroupa distribution), the coupled effect of IMF and [Na/Fe] on Na features is not negligible (see the upper-right panel of Fig. 1): for $\Gamma_b = 2.3$ and [Na/Fe] = 0.9 dex, one predicts an Na I1.14 line strength as high as for the case of a significantly bottom-heavy distribution ($\Gamma_b = 3.3$), and lower [Na/Fe]($\sim$0.6 dex). Note that this scenario would not work for a significantly heavier, single-segment IMF, supporting the conclusions of LB16. Our work also shows that the way of implementing the effect of [Na/Fe] in low-temperature stars will affect the NIR Na-sensitive line strengths, especially in the high-metallicity regime. However, the mismatch becomes significant (although still below the 10 per cent level) only for a bottom-heavy IMF.

The behaviour of the Na I2.21 index is perhaps even more complex. Meneses-Goytia et al. (2015) found that both their and CvD12a models are unable to match the larger Na I2.21 of massive ETGs (see also Röck et al. in preparation). Mármol-Queraltó et al. (2009) reported a significant correlation of Na I2.21 with the optical C4668 index in ETGs, suggesting a contribution of [C/Fe] to the index that would hamper its use to constrain IMF and [Na/Fe]. Such a scenario is disfavoured by our data, as XSG2 has significantly lower [C/Fe] and [α/Fe] than XSG1, but still has a high Na I2.21 line strength (see Section 5). Moreover, both Na I2.21 and Na I1.14 give consistent estimates of [Na/Fe], whereas the data for the central region of XSG2 are where our models match less well the observations. Thus, at the moment, the interpretation of Na I2.21 remains incomplete, and needs further investigations based on larger, homogeneous, samples.

The use of optical Na-sensitive lines to constrain the IMF has been recently discussed by Zieleniewski et al. (2015, hereafter ZHD15), based on new (literature) Na I8190 (NaD) data from the bulge of M31. The authors argue that, because of the lower (higher) sensitivity of Na I8190 (NaD) to IMF in the extended-MILES, with respect to the CvD12a models, one would infer a heavier IMF for the inner bulge of M31 with MILES, relative to CvD12a models, inconsistent with dynamical constraints (Saglia et al. 2010). Results from the two sets of models might be reconciled if either (i) Na I8190 is more sensitive to [Na/Fe], relative to NaD; or (ii) NaD decreases far more with [α/Fe], relative to Na I8190, in the MILES models. Indeed, neither of these two hypotheses is supported by our analysis, as the ratio of the responses to [α/Fe] (see Fig. 5) and [Na/Fe] (see Fig. 1) is quite similar between the two sets of models. However, one cannot constrain it in the regime of extreme [Na/Fe] overabundance, as might be the case for the bulge of M31 (for which CvD12a report a value of [Na/Fe] $\sim$ 1 dex). Another possibility is that the NaD line strengths used by ZHD15 – originally observed by Davidge (1991, 1997) at much lower resolution than Na I8190 – are, for some unknown reason, significantly underestimated. Further, homogeneous, observations of all Na features in the bulge of M31 (including Na I1.14 and Na I2.21), as well as the computation of extended-MILES models where *both* [α/Fe] and [Na/Fe] are varied *simultaneously*, would help elucidate these issues.

10 SUMMARY

In this work, we have performed, for the first time, a joint, radially extended analysis of the four most prominent Na-sensitive features in the optical and the NIR spectral range NaD, Na I λ8190Å, Na I λ1.14 μm, and Na I λ2.21 μm (NaD, Na I8190, Na I1.14, and Na I2.21, respectively), in two massive nearby ETGs (named XSG1 and XSG2), observed with the VLT/X-Shooter spectrograph at a high S/N across the optical+NIR spectral window. The analysis relies on a modified version of the extended-MILES stellar population models, covering the range from 0.35 to 5 μm, at moderately high, and uniform, spectral resolution (Vazdekis et al. 2012; Röck et al. 2015). By use of theoretical responses of [Na/Fe] to empirical stellar spectra, we compute a new set of (publicly available) population synthesis models, including a varying [Na/Fe]. For the first time, it is possible to assess the effect of [Na/Fe] on optical and NIR spectral features as a function of (total) metallicity and IMF, allowing for a wide abundance range (up to [Na/Fe] $\sim$ 1.2 dex). Our main results are the following.

(i) From a modelling point of view, we find that the effect of varying [Na/Fe] is strongly coupled to the IMF slope. For a bottom-heavy distribution, an increase of [Na/Fe] produces a stronger

variation of Na line strengths than for a Kroupa-like IMF. In other words, a bottom-heavy IMF boosts the effect of [Na/Fe], affecting, in particular, the NIR Na indices (Na I8190, Na I1.14, and Na I2.21), as the impact of [Na/Fe] increases with decreasing temperature for dwarf stars.

(ii) For XSG1, where line strengths are measured at different galactocentric distances, we find a significant negative radial gradient in all Na lines, although the error bars are larger for Na I2.21.

(iii) For the first time, our models allow us to explain *simultaneously* all four Na-sensitive line strengths in massive ETGs, and in particular the large values observed in Na I1.14 and Na I2.21.

(iv) To this effect, both a bottom-heavy IMF and a 'high' [Na/Fe] are required, in the central regions of both targets. The central best-fitting value of [Na/Fe] for XSG1 (XSG2) is ∼0.7 dex (0.5 dex). In XSG1, the radial IMF trend from Na-sensitive features is consistent with the constraints from TiO features shown in our previous work (LB16), although with larger error bars in the outermost galaxy regions.

(v) The radial trend of [Na/Fe] in XSG1 is similar to [α/Fe] and [C/Fe], featuring a constant value out to ∼0.5 R_e, followed by a lower [Na/Fe] (by ∼0.2 dex) in the outermost radial bin (∼0.8 R_e).

(vi) Considering the current uncertainties on theoretical atmosphere models (i.e. the lack of [Na/Fe]-enhanced models for cool stars, and LTE, rather than NLTE assumptions), all [Na/Fe] estimates should be taken as upper limits. For instance, modelling the response of cool stars to [Na/Fe] might lead to [Na/Fe] estimates mildly lower, by ∼0.1 dex, than those reported here.

In conclusion, while there are still open issues related to the interpretation of Na-sensitive absorption features in ETGs – requiring further developments of stellar population models – this work represents a significant leap forward with respect to previous studies, as for the first time we have shown that one can effectively match all prominent optical and NIR Na-sensitive features in massive galaxies, provided that a varying IMF, and non-solar abundance ratios are taken into account.

ACKNOWLEDGEMENTS

This research is based on observations made with ESO Telescopes at the Paranal Observatory under programmes ID 092.B-0378 and 094.B-0747 (PI: FLB). FLB acknowledges the Instituto de Astrofísica de Canarias for the kind hospitality when this project started. We thank Dr J. Alcalá for the insightful discussions and help with the reduction of X-Shooter spectra. We also thank Dr F. D'Antona and Dr M. Salaris for helpful discussions about Na production during different stages of stellar evolution. We thank the anonymous referee for his/her useful comments that helped us to improve our manuscript. We have made extensive use of the SDSS data base (http://www.sdss.org/collaboration/credits.html). MC acknowledges support from a Royal Society University Research Fellowship. We acknowledge support from grant AYA2013-48226-C3-1-P from the Spanish Ministry of Economy and Competitiveness (MINECO).

REFERENCES

Allende Prieto C., Hubeny I., Lambert D. L., 2003, ApJ, 591, 1192
Allende Prieto C. et al., 2008, AJ, 136, 2070
Alonso A., Arribas S., Martínez-Roger C., 1995, A&A, 297, 197
Alonso A., Arribas S., Martínez-Roger C., 1996, A&A, 313, 873
Alonso A., Arribas S., Martínez-Roger C., 1999, A&AS, 140, 261
Andrievsky S. M., Spite M., Korotin S. A., Cayrel R., Hill V., Françis P., 2007, A&A, 464, 1081
Asplund M., Grevesse N., Sauval A. J., Scott P., 2009, ARA&A, 47, 481
Barklem P. S., Piskunov N., O'Mara B. J., 2000, A&AS, 142, 467
Bautista M. A., 1997, A&AS, 122, 167
Bruls J. H. M. J., Rutten R. J., Shchukina N. G., 1992, A&A, 265, 237
Cappellari M., Emsellem E., 2004, PASP, 116, 138
Cappellari M. et al., 2012, Nature, 484, 485
Cappellari M. et al., 2013, MNRAS, 432, 1862
Carretta E., Bragaglia A., Gratton R., Lucatello S., 2009, A&A, 505, 139
Cassisi S., Castellani V., Ciarcelluti P., Piotto G., Zoccali M., 2000, MNRAS, 315, 679
Cassisi S., Salaris M., Castelli F., Pietrinferni A., 2004, ApJ, 616, 498
Castelli F., Kurucz R. L., 2004, preprint (astro-ph/0405087)
Cenarro A. J., Cardiel N., Gorgas J., Peletier R. F., Vazdekis A., Prada F., 2001, MNRAS, 326, 959
Cenarro A. J., Gorgas J., Vazdekis A., Cardiel N., Peletier R. F., 2003, MNRAS, 339, L12
Cenarro A. J. et al., 2007, MNRAS, 374, 664
Cervantes J. L., Vazdekis A., 2009, MNRAS, 392, 691
Chabrier G., 2003, PASP, 115, 763
Chabrier G., Hennebelle P., Charlot S., 2014, ApJ, 796, 75
Chieffi A., Limongi M., 2004, ApJ, 608, 405
Coelho P., Barbuy B., Melendez J., Schiavon R., Castilho B., 2005, A&A, 443, 735
Coelho P., Bruzual G., Charlot S., Weiss A., Barbuy B., Ferguson J. W., 2007, MNRAS, 382, 498
Colucci J. E., Bernstein R. A., Cohen J., 2014, ApJ, 797, 116
Conroy C., van Dokkum P., 2012a, ApJ, 747, 69 (CvD12)
Conroy C., van Dokkum P., 2012b, ApJ, 760, 71 (CvD12b)
Conroy C., Graves G. J., van Dokkum P. G., 2014, ApJ, 780, 33
Cunto W., Mendoza C., Ochsenbein F., Zeippen C. J., 1993, A&A, 275, L5
Cushing M. C., Rayner J. T., Vacca W. D., 2005, ApJ, 623, 1115
Davidge T. J., 1991, AJ, 101, 884
Davidge T. J., 1997, AJ, 113, 985
Ferreras I., La Barbera F., de la Rosa I. G., Vazdekis A., de Carvalho R. R., Falcón-Barroso J., Ricciardelli E., 2013, MNRAS, 429, L15 (F13)
Ferreras I., Weidner C., Vazdekis A., La Barbera F., 2015, MNRAS, 448, 82
Gehren T., Shi J. R., Zhang H. W., Zhao G., Korn A. J., 2006, A&A, 451, 1065
Girardi L., Bressan A., Bertelli G., Chiosi C., 2000, A&AS, 141, 371
Grevesse N., Sauval A. J., 1998, Space Sci. Rev., 85, 161
Hopkins P. F., 2013, MNRAS, 433, 170
Irwin A. W., 1981, ApJS, 45, 621
Jeong H., Yi S. K., Kyeong J., Sarzi M., Sung E.-C., Oh K., 2013, ApJS, 208, 7
Kobayashi C., Umeda H., Nomoto K., Tominaga N., Ohkubo T., 2006, ApJ, 653, 1145
Koesterke L., 2009, in Hubeny I., Stone J. M., MacGregor K., Werner K., eds, AIP Conf. Proc. Vol. 1171, Recent Directions in Astrophysical Quantitative Spectroscopy and Radiation Hydrodynamics. Am. Inst. Phys., New York, p. 73
Koesterke L., Allende Prieto C., Lambert D. L., 2008, ApJ, 680, 764
Kroupa P., 2001, MNRAS, 322, 231
La Barbera F., de Carvalho R. R., Kohl-Moreira J. L., Gal R. R., Soares-Santos M., Capaccioli M., Santos R., Sant'Anna N., 2008, PASP, 120, 681
La Barbera F., de Carvalho R. R., de la Rosa I. G., Lopes P. A. A., Kohl-Moreira J. L., Capelato H. V., 2010, MNRAS, 408, 1313
La Barbera F., Ferreras I., de Carvalho R. R., Bruzual G., Charlot S., Pasquali A., Merlin E., 2012, MNRAS, 426, 2300
La Barbera F., Ferreras I., Vazdekis A., de la Rosa I. G., de Carvalho R. R., Trevisan M., Falcón-Barroso J., Ricciardelli E., 2013, MNRAS, 433, 3017 (LB13)
La Barbera F., Ferreras I., Vazdekis A., 2015, MNRAS, 449, L137
La Barbera F., Vazdekis A., Ferreras I., Pasquali A., Cappellari M., Martín-Navarro I., Schönebeck F., Falcón-Barroso J., 2016, MNRAS, 457, 1468 (LB16)

Leier D., Ferreras I., Saha P., Charlot S., Bruzual G., La Barbera F., 2016, MNRAS, 459, 3677
Lind K., Asplund M., Barklem P. S., Belyaev A. K., 2011, A&A, 528, 103
McConnell N. J., Lu J. R., Mann A. W., 2016, ApJ, 821, 39
Maraston C., 2005, MNRAS, 362, 799
Marigo P., Girardi L., Bressan A., Groenewegen M. A. T., Silva L., Granato G. L., 2008, A&A, 482, 883
Mármol-Queraltó E. et al., 2009, ApJ, 705, 199
Martín-Navarro I., La Barbera F., Vazdekis A., Falcón-Barroso J., Ferreras I., 2015a, MNRAS, 447, 1033
Martín-Navarro I., La Barbera F., Vazdekis A., Ferré-Mateu A., Trujillo I., Beasley M. A., 2015b, MNRAS, 451, 1081
Martín-Navarro I. et al., 2015c, ApJ, 806, L31
Meneses-Goytia S., Peletier R. F., Trager S. C., Vazdekis A., 2015, A&A, 582, A97
Mészáros Sz. et al., 2012, AJ, 144, 120
Modigliani A. et al., 2010, in Silva D. R., Peck A. B., Soifer T., eds, Proc. SPIE Conf. Ser. Vol. 7737, Observatory Operations: Strategies, Processes, and Systems III. SPIE, Bellingham, p. 773728
Nahar S. N., 1995, A&A, 293, 967
Navarro-González J., Ricciardelli E., Quilis V., Vazdekis A., 2013, MNRAS, 436, 3507
Oser L., Ostriker J. P., Naab T., Johansson P. H., Burkert A., 2010, ApJ, 725, 2312
Padoan P., Nordlund Å., 2002, ApJ, 576, 870
Pietrinferni A., Cassisi S., Salaris M., Castelli F., 2004, ApJ, 612, 168
Pietrinferni A., Cassisi S., Salaris M., Castelli F., 2006, ApJ, 642, 797
Rayner J. T., Toomey D. W., Onaka P. M., Denault A. J., Stahlberger W. E., Vacca W. D., Cushing M. C., Wang S., 2003, PASP, 115, 362
Reimers D., 1977, A&A, 57, 395
Röck B., Vazdekis A., Peletier R. F., Knapen J. H., Falcón-Barroso J., 2015, MNRAS, 449, 2853
Röck B., Vazdekis A., Ricciardelli E., Peletier R. F., Knapen J. H., Falcón-Barroso J., 2016, A&A, 589, 73
Saglia R. P. et al., 2010, A&A, 509, A61
Salpeter E. E., 1955, ApJ, 121, 161
Sánchez-Blázquez P. et al., 2006, MNRAS, 371, 703
Schönebeck F., Puzia T. H., Pasquali A., Grebel E. K., Kissler-Patig M., Kuntschner H., Lyubenova M., Perina S., 2014, A&A, 572, 13
Silva D. R., Kuntschner H., Lyubenova M., 2008, ApJ, 674, 194
Simard L., Mendel J. T., Patton D. R., Ellison S. L., McConnachie A. W., 2011, ApJS, 196, 11
Smith R. J., Lucey J. R., 2013, MNRAS, 434, 1964
Smith R. J., Alton P., Lucey J. R., Conroy C., Carter D., 2015, MNRAS, 454, 71 (SAL15)
Sparks W. B., Carollo C. M., Macchetto F., 1997, ApJ, 486, 253
Spiniello C., Trager S. C., Koopmans L. V. E., Chen Y. P., 2012, ApJ, 753, L32
Spiniello C., Trager S. C., Koopmans L. V. E., Conroy C., 2014, MNRAS, 438, 1438
Spiniello C., Trager S. C., Koopmans L. V. E., 2015, ApJ, 803, 87
Spinrad H., Taylor B. J., 1971, ApJS, 22, 445
Thomas D., Maraston C., Bender R., 2003, MNRAS, 339, 897
Thomas D., Maraston C., Johansson J., 2011, MNRAS, 412, 2183 (TMJ11)
Trager S. C., Worthey G., Faber S. M., Burstein D., González J. J., 1998, ApJS, 116, 1
Treu T., Auger M. W., Koopmans L. V. E., Gavazzi R., Marshall P. J., Bolton A. S., 2010, ApJ, 709, 1195
Tripicco M. J., Bell R. A., 1995, AJ, 110, 3035
Tsuji T., 1973, A&A, 23, 411
Valdes F., Gupta R., Rose J. A., Singh H. P., Bell D. J., 2004, ApJS, 152, 251
van Dokkum P. G., Conroy C., 2010, Nature, 468, 940
Vazdekis A., Casuso E., Peletier R. F., Beckman J. E., 1996, ApJS, 106, 307
Vazdekis A., Peletier R. F., Beckman J. E., Casuso E., 1997, ApJS, 111, 203
Vazdekis A., Cenarro A. J., Gorgas J., Cardiel N., Peletier R. F., 2003, MNRAS, 340, 1317
Vazdekis A., Sánchez-Blázquez P., Falcón-Barroso J., Cenarro A. J., Beasley M. A., Cardiel N., Gorgas J., Peletier R. F., 2010, MNRAS, 404, 1639
Vazdekis A., Ricciardelli E., Cenarro A. J., Rivero-González J. G., Díaz-Garcá L. A., Falcón-Barroso J., 2012, MNRAS, 424, 157
Vazdekis A. et al., 2015, MNRAS, 449, 1177 (V15)
Ventura P., Di Criscienzo M., Carini R., D'Antona F., 2013, MNRAS, 431, 3642
Vernet J. et al., 2011, A&A, 536, A105
Weidner C., Ferreras I., Vazdekis A., La Barbera F., 2013, MNRAS, 435, 2274
Worthey G., Tang B., Serven J., 2014, ApJ, 783, 20
Zieleniewski S., Houghton R. C. W., Thatte N., Davies R. L., 2015, MNRAS, 452, 597 (ZHD15)

APPENDIX A: EFFECT OF LOW-TEMPERATURE STARS ON [Na/Fe]-ENHANCED MODELS

Since theoretical stellar spectra do not cover temperatures cooler than $T_{\rm eff} = 3500$ K (see Section 3.2), for stars with $T_{\rm eff} < 3500$ K in the empirical stellar library (see Section 3), we applied differential corrections for [Na/Fe] by assuming $T_{\rm eff} = 3500$ K. This is a rather conservative approach, as Na-sensitive absorption lines strengthen with decreasing temperature. Hence, our [Na/Fe]-enhanced SSP spectra might underestimate the sensitivity of Na indices to [Na/Fe], especially for a bottom-heavy IMF. To assess the impact of $T_{\rm eff}$ on our results, we compute a set of models for which we linearly *extrapolate* the [Na/Fe] differential corrections to $T_{\rm eff} < 3500$ K. For each stellar spectrum, we use our interpolation algorithm (see Section 3) to compute differential corrections (at each wavelength in the spectrum) in the temperature range from 3500 to 4500 K, for the chosen [Fe/H] and $\log g$. The differential correction is linearly extrapolated, with respect to $T_{\rm eff}$, at the desired temperature value. We compute the [Na/Fe]-enhanced SSP models by exchanging the input stellar library spectra by the corresponding [Na/Fe]-enhanced ones, i.e. exactly in the same way as for the base model SSPs. We finally assemble the SSP spectra as described in Röck et al. (2016).

Fig. A1 compares Na-MILES model predictions with those of $T_{\rm eff}$-extrapolated models, for [Na/Fe] = 0.6 dex. As expected, the effect of the extrapolation is to increase the Na-sensitive line strengths. The variation is very small for NaD and Na I8190, while it is somewhat larger, albeit still small, for the NIR Na I1.14 and Na I2.21 indices. Note that the extrapolation affects more the high-metallicity (i.e. lower-temperature) regime as well as models with a bottom-heavy IMF. Since the corresponding variation of line strengths is lower than ∼10 per cent, fitting observed line strengths with $T_{\rm eff}$-extrapolated, rather than our reference, Na-MILES models give very similar results to those presented in Section7. The most noticeable difference is that for $T_{\rm eff}$-extrapolated models we infer mildly lower (by ∼0.1 dex) [Na/Fe] estimates than those in Fig. 4, not affecting any of the conclusions of our work.

APPENDIX B: COMPARISON OF EXTENDED-MILES AND CVD12 MODEL PREDICTIONS

Fig. B2 compares predictions of Na-sensitive line strengths for CvD12 and extended-MILES stellar population models. The figure is similar to Fig. 1, showing the Na line strengths as a function of [MgFe]′. However, since CvD12 models include only SSPs with either Chabrier or unimodal (i.e. single-segment) IMF, Fig. B2 plots the extended-MILES models with a varying unimodal, rather than bimodal, IMF slope, with $0.3 \leq \Gamma \leq 2.3$. For CvD12 models, we plot

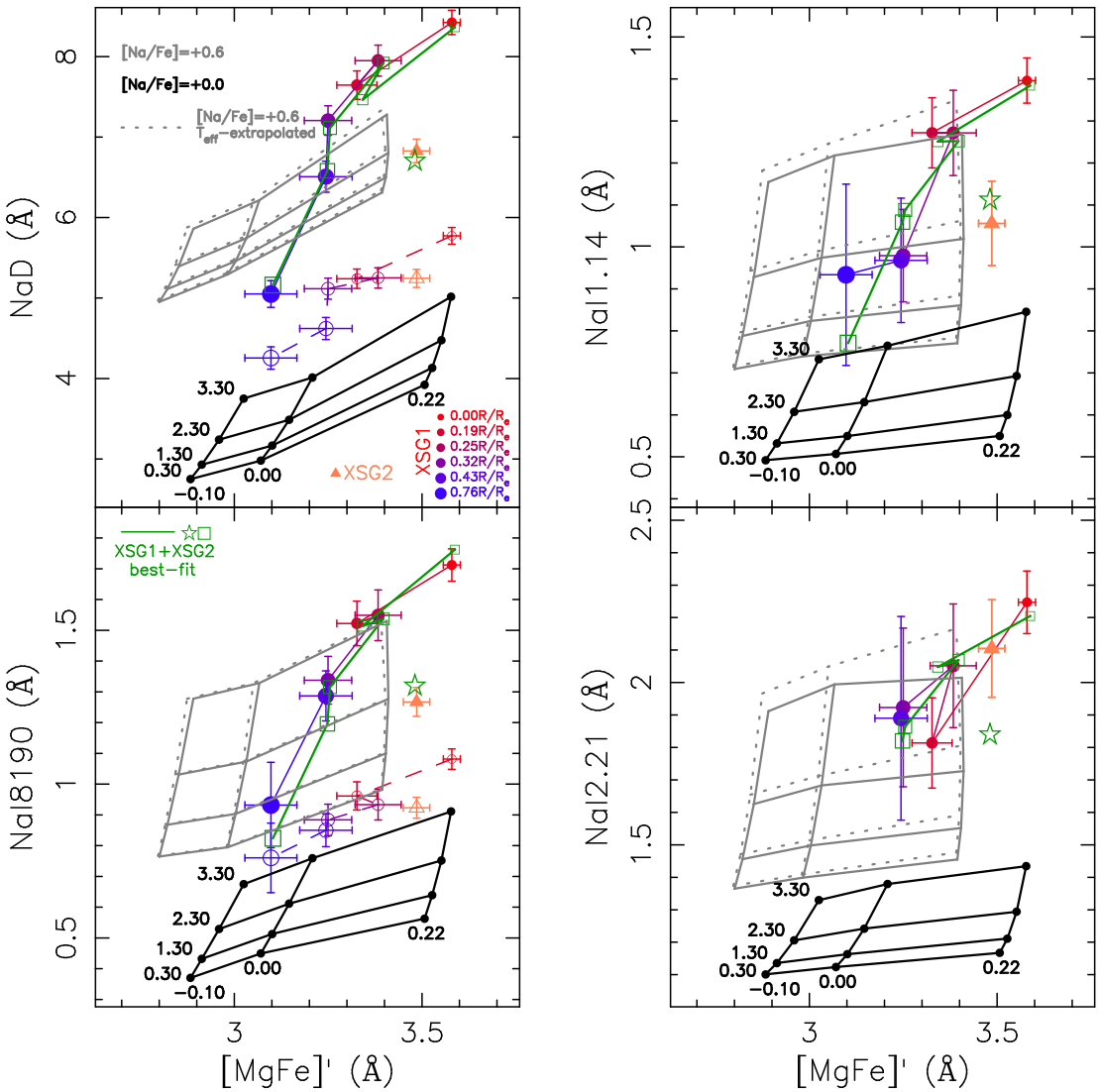

Figure A1. Same as Fig. 1, but plotting only models with [Na/Fe] = 0 (black grids) and [Na/Fe] = 0.6 dex (grey grids), respectively, with dotted grids showing the case where in the low-temperature regime (<3500 K) the effect of Na abundance on stellar atmospheres is linearly extrapolated, rather than assumed to be the same as for $T_{\rm eff}$ = 3500 K. Note that the effect of $T_{\rm eff}$ is almost negligible for NaD and Na I8190, while for Na I1.14 and Na I2.21 the extrapolation increases the model line strengths, in particular for models with high metallicity, and bottom-heavy IMF. As a result, one would infer somewhat lower Na abundances (by ∼0.1 dex) than those reported in the upper panel of Fig. 4.

predictions for either a Chabrier or a unimodal, bottom-heavy, IMF with $\Gamma = 2.3$ (see grey stars in the figure). As far as the dwarf-to-giant ratio or the stellar mass-to-light ratio are concerned, the case of a unimodal IMF with the slope $\Gamma \sim 0.8$ roughly corresponds to an Milky-Way (MW)-like distribution (see, e.g. F13 and LB13). Hence, the predictions of CvD12 models for a Chabrier distribution can be compared to those for extended-MILES models with $\Gamma \sim 0.8$.

Fig. B2 shows that the sensitivity of Na lines to the IMF differs significantly between CvD12 and extended-MILES models. The NaD (Na I8190) is more (less) sensitive to IMF in extended-MILES than CvD12 models, in agreement with Spiniello et al. (2015) and ZHD15. The difference is even more pronounced for Na I1.14 (see SAL15), where CvD12 features have a stronger sensitivity than the extended-MILES models. For Na I2.21, predictions from different models are consistent, though the effect of IMF variations is slightly larger for CvD12 than extended-MILES models. The origin of such a discrepancy is still unclear, but mostly arises from the way different models attach stars to the isochrones, while other ingredients (e.g. the adopted isochrones) will likely play a secondary role (see Spiniello et al. 2015). For the purpose of this work, we want to test the impact of differences in the sensitivity of the models to the IMF on the derivation of the IMF slopes and [Na/Fe] abundance ratios in XSG1 and XSG2. To this effect, we have first rescaled Na-MILES models to match the IMF response of CvD12 models. For both sets of models, we compute the IMF sensitivity of Na lines as follows:

$$\gamma_{{\rm Na}_j} = {\rm Na}_j(\Gamma = 2.3) - {\rm Na}_{j,{\rm ref}}, \qquad \text{(B1)}$$

where index j defines a given Na line (see Section 6), $\mathrm{Na}_{j,\,\mathrm{ref}}$ are line strengths computed for an MW-like IMF, i.e. a Chabriér (Kroupa) distribution for CvD12 (MILES) models. For both sets of models, $\mathrm{Na}_j(\Gamma = 2.3)$ are line strengths of an SSP model having unimodal, bottom-heavy, IMF with the slope $\Gamma = 2.3$. All line strengths in equation (B1) are computed for SSP models with solar metallicity and an (old) age of ∼13 Gyr. The values of γ_j as well as the *relative* responses of Na lines to IMF (defined as $\gamma_j/\mathrm{Na}_{j,\,\mathrm{ref}}$) are reported in Table B1.

Table B1. Response of Na features to IMF (see equation B1) for CvD12 and extended-MILES SSP models (columns 2 and 3, respectively). Values in parentheses are relative responses, defined as $\gamma_j/\mathrm{Na}_{j,\,\mathrm{ref}}$ (see the text).

Index	$\gamma_{j\mathrm{CvD}}$ (Å)	$\gamma_{j\mathrm{MILES}}$ (Å)
(1)	(2)	(3)
NaD	0.41(0.13)	0.92(0.28)
Na I 8190	0.63(1.40)	0.23(0.43)
Na I 1.14	0.73(1.34)	0.40(0.73)
Na I 2.21	0.41(0.37)	0.37(0.32)

For each value of [Na/Fe] (0, 0.3, 0.6, 0.9, 1.2, see Section 3), we have then rescaled Na-MILES models, for bimodal distributions, as follows:

$$\mathrm{Na}'_j(\Gamma_\mathrm{b}) = \mathrm{Na}_{j,\mathrm{ref}} + \frac{\gamma_{j,\mathrm{CvD}}}{\gamma_{j,\mathrm{MILES}}} \cdot \left[\mathrm{Na}_j(\Gamma_\mathrm{b}) - \mathrm{Na}_{j,\mathrm{ref}}\right]. \qquad \text{(B2)}$$

The rescaled models are shown as grey dashed grids in Fig. B1, for the case with [Na/Fe] = 0. As expected, the effect is to increase (decrease) significantly the IMF sensitivity of Na I 8190 and Na I 1.14 (NaD), while leaving the Na I 2.21 grid almost unaltered. Using similar equations as (B1) and (B2), we further modified the IMF-rescaled Na-MILES models in order to match also the sensitivity of CvD12 models to [Na/Fe]. Hereafter, we refer to these modified models as CvD-matched (Na-MILES) models.

We emphasize that, for the purpose of this work, we do not aim at discussing the origin of differences among Na-MILES and CvD12 models, but rather to test the possible impact of such differences on our results. Fig. B2 compares best-fitting IMF slopes and [Na/Fe] ratios obtained with Na-MILES models (green curves in the figure; see case A in Table 6) to those obtained for CvD-matched models (brown curves in the figure). In the latter case, we have applied no IMF constraint for XSG1 (see Section 6.4). Interestingly, we get similar results from Na-MILES and CvD-matched models, in that

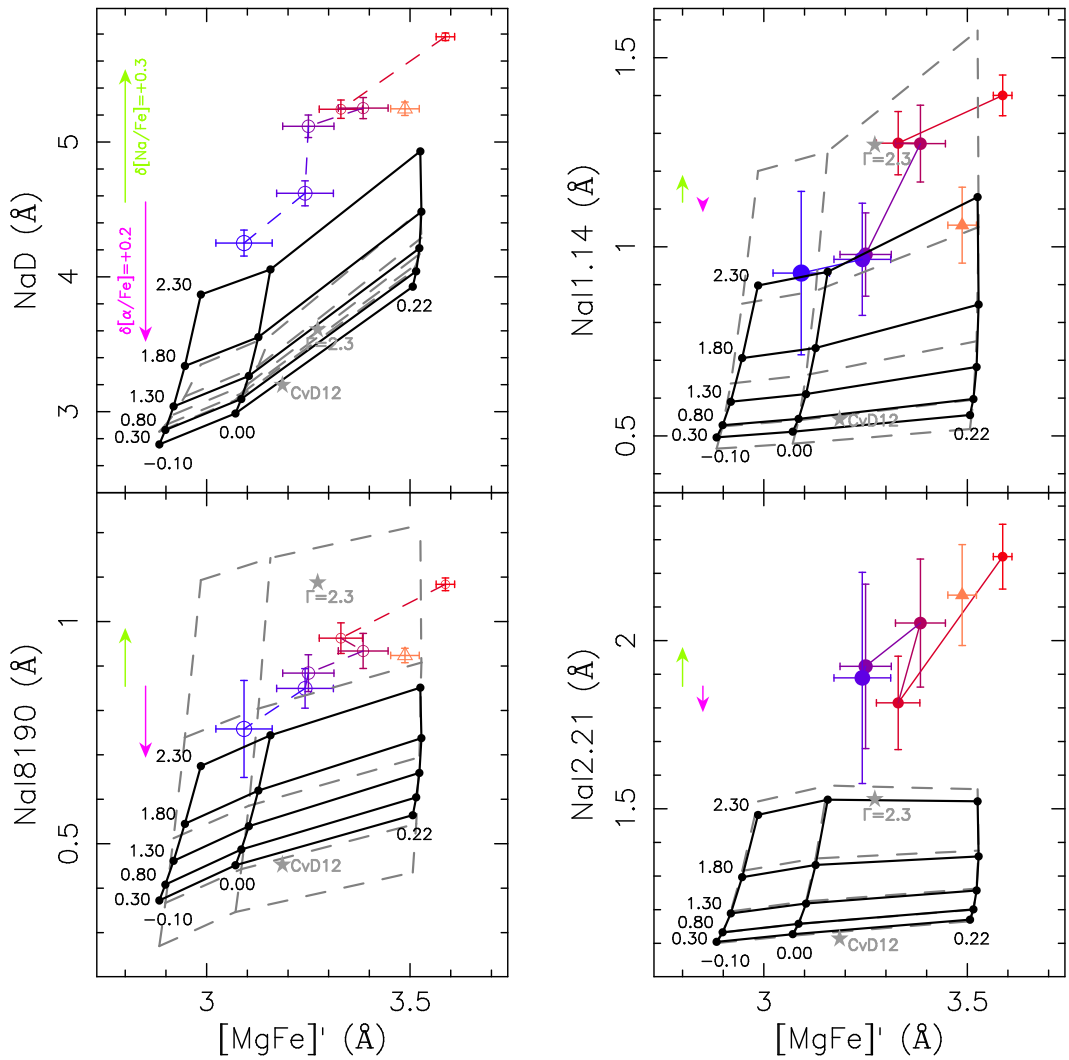

Figure B1. Same as Fig. 1, but plotting predictions for unimodal, rather than bimodal, extended-MILES SSPs. The NaD and Na I 8190 line strengths are not corrected to [α/Fe] = 0 (see filled circles and triangles in the left-hand panels of Fig. 1). Black grids correspond to models with [Na/Fe] = 0, varying metallicity ([M/H] = −0.1, 0, +0.22) and unimodal IMF slope (Γ = +0.3, 0.80, 1.30, 1.80, 2.30), for an age of 11.2 Gyr. Note that Γ = 1.35 corresponds to the Salpeter IMF, while Γ ∼ 0.8 roughly matches the mass-to-light ratio for a Kroupa-like IMF. To make the figure more clear, only models with [Na/Fe] = 0 are plotted. Grey grids are extended-MILES model predictions rescaled to match the IMF response of CvD12 models (see the text). Grey stars are predictions from publicly available CvD12 SSP models, with solar metallicity, age of 13.5 Gyr, and Chabrier and unimodal bottom-heavy (Γ = 2.3) IMFs, respectively. In each panel, light-green and magenta arrows show the effect of increasing [α/Fe] ([Na/Fe]) by +0.2 dex (+0.3 dex) in CvD12 models.

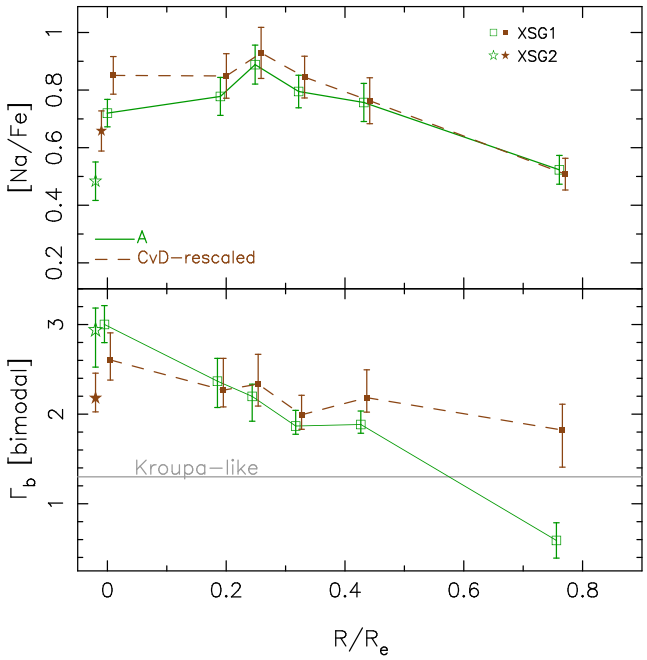

Figure B2. [Na/Fe] ratios (top) and IMF slopes (bottom) as a function of galactocentric distance, for XSG1 (squares) and XSG2 (stars), respectively. Green open symbols are the same as in the upper panel of Figs 3 and 4, respectively. Brown filled symbols, connected by a dashed line, are results obtained by fitting observed line strengths with Na-MILES models rescaled to match the response of CvD12 models to IMF and [Na/Fe] (see the text). Note that this approach is only meant to test the robustness of our results against uncertainties on state-of-the-art stellar population models.

we need high [Na/Fe] ratios, as well as a bottom-heavy IMF in the innermost radial bins, as well as an IMF radial gradient for XSG1, to fit our data. However, in the four inner radial bins of XSG1, as well as for the central bin of XSG2, we tend to infer higher [Na/Fe], and lower Γ_b, for CvD-matched than Na-MILES models. For the innermost bin of XSG1 (XSG2), [Na/Fe] is ∼0.15 dex (∼0.2 dex) higher, while Γ_b is ∼0.4 (∼0.7) lower, for CvD12-matched than Na-MILES. In the outermost bins of XSG1, results are similar for both sets of models, with lower [Na/Fe] and a lighter IMF slope,[17] than in the innermost radial bins. In other words, CvD12-matched models give a shallower IMF (steeper [Na/Fe]) trend than Na-MILES models, with a somewhat lighter, yet bottom-heavy, IMF slope in the innermost radial bins of both our targets. Note that, in a somewhat similar way to these results, Spiniello et al. (2015) found that CvD12 and MILES models tend to predict similar trends of IMF slope with velocity dispersion in ETGs, though the MILES models favour slightly higher slopes for the most massive ETGs. In any case, the main point of this work is that our results are robust against uncertainties of state-of-the-art stellar population models on the IMF response of Na-sensitive features.

[17] Note that when no IMF constraints are imposed for XSG1, we get significantly larger error bars on the IMF slope for Na-MILES (see cases B and E in Fig. 3) than CvD-matched models (brown curve in Fig. B2), in particular for the outermost radial bins. This happens as for CvD-matched models, Na I 8190 and Na I 1.14 have significantly larger sensitivity to IMF than [Na/Fe], while for Na-MILES, all Na features have significant sensitivity to both IMF and [Na/Fe] (see Section 7.1), implying a stronger degeneracy between IMF and [Na/Fe] (hence larger error bars) in the latter case.

This paper has been typeset from a TEX/LATEX file prepared by the author.